MNRAS **000**, 1–18 (2020) Preprint 14 September 2021 Compiled using MNRAS LATEX style file v3.0

Infrared Colours and Spectral Energy Distributions of Hard X-ray Selected Obscured and Compton-thick AGN

Ece Kilerci Eser,[1]★ T. Goto,[2] T. Güver,[1] A. Tuncer,[1,3] O. H. Ataş[1,3]
[1]*Istanbul University, Science Faculty, Department of Astronomy and Space Sciences, Beyazıt, 34119, Istanbul, Turkey*
[2]*Institute of Astronomy , National Tsing Hua University, No. 101, Section 2, Kuang-Fu Road, Hsinchu, 30013, Taiwan*
[3]*Graduate School of Science and Engineering, Department of Astronomy and Space Sciences, Istanbul University, Istanbul, Turkey*

Accepted XXX. Received YYY; in original form ZZZ

ABSTRACT

We investigate infrared colours and spectral energy distributions (SEDs) of 338 X-ray selected AGN from *Swift*-BAT 105-month survey catalogue that have *AKARI* detection, in order to find a new selection criteria for Compton-thick AGN. By combining data from Galaxy Evolution Explore (*GALEX*), Sloan Digital Sky Survey (SDSS) Data Release 14 (DR14), Two Micron All Sky Survey (2MASS), Wide-field Infrared Survey Explorer (*WISE*), *AKARI* and *Herschel* for the first time we perform ultraviolet (UV) to far-infrared (FIR) SED fitting 158 *Swift*-BAT AGN by CIGALE and constrain the AGN model parameters of obscured and Compton-thick AGN. The comparison of average SEDs show while the mid-IR (MIR) SEDs are similar for the three AGN populations, optical/UV and FIR regions have differences. We measure the dust luminosity, the pure AGN luminosity and the total infrared (IR) luminosity. We examine the relationships between the measured infrared luminosities and the hard X-ray luminosity in the 14-195 keV band. We show that the average covering factor of Compton-thick AGN is higher compared to the obscured and unobscured AGN. We present a new infrared selection for Compton-thick AGN based on MIR and FIR colours ($[9\mu\mathrm{m} - 22\mu\mathrm{m}] > 3.0$ and $[22\mu\mathrm{m} - 90\mu\mathrm{m}] < 2.7$) from *WISE* and *AKARI*. We find two known Compton-thick AGN that are not included in the *Swift*-BAT sample, and conclude that MIR colours covering 9.7μm silicate absorption and MIR continuum can be a promising new tool to identify Compton-thick AGN.

Key words: galaxies: active – quasars:general –infrared: galaxies

1 INTRODUCTION

Active galactic nuclei (AGN) are the mass accreting supermassive black holes residing at the centres of nearly all massive galaxies. Recent studies show that AGN that are obscured by gas and dust may make up a non-negligible fraction of the AGN population (e.g., Hickox et al. 2007; Treister et al. 2010; Assef et al. 2013, 2015; Mateos et al. 2017). Obscured AGN are important to understand the full growing black hole population and the influence of black holes on the host galaxy (e.g., Hopkins et al. 2008). These sources are important to understand the accretion history of super massive black holes via the cosmic X-ray background radiation (e.g., Ueda et al. 2014). It is still unknown how much obscured AGN are there in the Universe. The number of low luminosity or obscured AGN is critical for our understanding of galaxies (e.g., Hickox & Alexander 2018). Therefore, it is important to find new techniques to identify obscured AGN.

The structure of an AGN mainly composed of a central super massive black hole, an accretion disc (Shakura & Sunyaev 1973) and a corona (e.g., Czerny & Elvis 1987; Zheng et al. 1997; Telfer et al. 2002; Done et al. 2012; Jin et al. 2012; Mehdipour et al. 2011, 2015). The accretion disc and the corona in its immediate vicinity produce the primary optical-UV and X-ray continuum emission (e.g., Sanders et al. 1989; Marconi et al. 2004; Suganuma et al. 2006). This central engine is embeded within the IR emitting dusty structure the so called torus (e.g., Antonucci 1993; Lawrence 1991; Simpson 2005; Hönig & Beckert 2007; García-Burillo et al. 2016). AGN that can be identified by their blue continuum and broad and/or narrow emission lines in the optical are often referred as 'Type 1' (e.g., Antonucci 1993). Once the AGN signatures can not be detected in the optical spectrum, then its refereed as a 'Type 2' or obscured AGN (e.g., Antonucci

★ E-mail: ecekilerci@phys.nthu.edu.tw (EKE)

1993). Obscured AGN may show narrow line emission or no emission at all depending on the degree of obscuration which is dictated by the geometrical structure of the dusty torus or the strength of the host galaxy emission (e.g., Hickox & Alexander 2018). Since they are mostly absorbed in the optical and soft X-rays, obscured AGN can mostly be identified in hard X-rays (e.g., Brandt & Alexander 2015) and infrared (IR) (e.g., Stern et al. 2005; Mateos et al. 2012; Assef et al. 2013; Hickox et al. 2017). In terms of the measured Hydrogen column density (N_H) from the X-ray spectra AGN can be classified as: (i) unobscured (log $N_H \leq 22.0$); (ii) obscured ($22.0 < \log N_H \leq 24.0$), and (iii) Compton-thick (CT) ($\log N_H \geq 24.0$).

In the mid-IR AGN have characteristic emission, that is produced by the circumnuclear dust heated by the optical/UV/X-ray radiation from the central engine. Therefore it is a common practice to use IR emission to separate AGN from starburst/normal galaxies (e.g., Stern et al. 2012; Mateos et al. 2013; Lansbury et al. 2014; Huang et al. 2017; Ichikawa et al. 2019). The mid-IR dust emission of an AGN is in the form of power-law with different slopes for Type 1 and Type 2 (Alonso-Herrero et al. 2006; Donley et al. 2007, 2008). IR power-law selection has been used to select AGN with *WISE* colours ([3.4μm-4.6μm] versus [4.6μm-12μm]) for AGN at low redshift ($z \leq 0.5$) (Mateos et al. 2012, 2013). *Spitzer* IRAC flux ratios ([8μm-4.5μm] versus [5.8μm- 3.6μm]) have been used as a reliable method to select AGN at higher redshift ($z \sim 1, 2$) (Lacy et al. 2004; Stern et al. 2005; Donley et al. 2008, 2012). Many AGN selection criteria have been shown and applied in other studies (Jarrett et al. 2013; Stern et al. 2012; Assef et al. 2013). Millions of AGN have been selected from All-WISE using the criteria of Mateos et al. (2012). The completeness of IR colour AGN selection is highly complete for luminous Type 1 AGN and moderately complete for Type 2 AGN (Mateos et al. 2012; Lansbury et al. 2017). It has been showed that (Mateos et al. 2013; Rovilos et al. 2014) obscured AGN and CT AGN candidates meet the MIR-selection criteria of Stern et al. (2012); Mateos et al. (2013); Lansbury et al. (2014). These colours mainly identify obscured AGN; however this colour selection has been combined with N_H classification only in a few studies (Mateos et al. 2013; Rovilos et al. 2014). In this work we focus on selecting obscured AGN with a new IR colour criteria.

Since MIR and the X-rays radiation originate from the AGN the two radiation is expected to be correlated. The relation between the mid-IR and X-ray emission has been an important tool to gain information about the AGN physics (e.g., Krabbe et al. 2001; Lutz et al. 2004; Ramos Almeida et al. 2007; Horst et al. 2008; Fiore et al. 2009; Gandhi et al. 2009; Fiore et al. 2009; Levenson et al. 2009; Asmus et al. 2011; Mason et al. 2012; Sazonov et al. 2012; Matsuta et al. 2012; Ichikawa et al. 2012; Asmus et al. 2015; Mateos et al. 2015; García-Bernete et al. 2016; Ichikawa et al. 2017; Chen et al. 2017; Ichikawa et al. 2019). The mid-IR and X-ray relation initially established for the 2-10 keV X-ray band, due to the technical limitations of the former X-ray telescopes. Once the hard X-ray telescopes like *Swift* and *INTEGRAL* become available the mid-IR and X-ray relation extended to the 14-195 keV ultra-hard X-ray regime (e.g., Mullaney et al. 2011; Matsuta et al. 2012; Ichikawa et al. 2012; Sazonov et al. 2012; Asmus et al. 2015; Ichikawa et al. 2017). Ichikawa et al. (2012) investigated the MIR and FIR properties of the AGN in the *Swift*/BAT nine-month catalog (Tueller et al. 2008) and find a good correlation between the MIR and X-ray luminosities. Ichikawa et al. (2017) and Ichikawa et al. (2019) studied the IR properties of the AGN in 70-month *Swift*/BAT sample in a great detail. Ichikawa et al. (2019) analysed IR SEDs and estimated AGN contribution to the 12μm, MIR, and total IR luminosities. They show a significant luminosity correlation between the MIR and 14-150 keV bands. Although IR colours and properties of the hard X-ray selected AGN in the previous *Swift*-BAT samples have been extensively studied, these literature studies Ichikawa et al. (2012, 2017, 2019) have not investigated a possible Compton-thick AGN selection based on the MIR and FIR colours which is the main goal of this study.

In this work, we combine the IR colours with the measured N_H of the X-ray selected AGN and present a new Compton-thick AGN selection criteria that allowed us to select Compton-thick AGN candidates from the *AKARI* all-sky survey catalogue. We also aim to constrain the AGN model parameters of obscured and CT AGN, within the limitations imposed by the model assumptions in CIGALE, the available broadband photometry, and the fitting procedure. The structure of this paper is as follows. In sections 2 and 3 we present the sample selection and data, respectively. We describe sed analysis of obscured and CT AGN in our sample in section 4. We compare average SEDs of unobscured, obscured and CT AGN in §5.1. In section 5.2 we present the correlations between the hard X-ray luminosity and the pure AGN luminosity in the IR band and dust luminosity. We show the N_H dependence of IR colours in section 5.3. In section 5.4 we present a new IR colour selection criteria for CT AGN. We summarise our conclusions in §6. We adopt a cosmology with $H_0 = 72\,\mathrm{km\,s^{-1}\,Mpc^{-1}}$, $\Omega_\Lambda = 0.7$ and $\Omega_m = 0.3$ and use the base 10 logarithm.

2 SAMPLE SELECTION

The *Swift* observatory (Gehrels et al. 2004) scans the whole sky at 14–195 keV with the wide-field Burst Alert Telescope (BAT; Barthelmy et al. 2005). With its continuous all-sky survey, *Swift*-BAT identified several hard-X-ray selected AGN in the local Universe (e.g., Tueller et al. 2008; Baumgartner et al. 2013; Ricci et al. 2017a; Oh et al. 2018). The most recent data release of *Swift*-BAT (105-month, Oh et al. 2018) includes 947 hard X-ray selected non-beamed AGN. To investigate the mid-IR and far-IR colours of the hard X-ray selected obscured and CT AGN we select the 947 non-beamed AGN from *Swift*-BAT 105-month survey catalogue (Oh et al. 2018). We cross-match these hard X-ray selected AGN based on their optical counter part coordinates with *AKARI*/FIS all-sky survey bright source catalogue version 2[1] (Yamamura et al. 2018) within a radius of 20 arcsec. We find *AKARI* 90 μm detection for 378 AGN. 90 μm detection is near the peak of the far-IR dust emission near 100 μm, and especially the 140 μm and 160 μm

[1] http://www.ir.isas.jaxa.jp/AKARI/Archive/Catalogues/FISBSCv2/

bands are crucial to constrain the dust emission peak and measure better IR luminosity. Among these AGN only 332 have detected in three *AKARI* bands at 90 μm, 140 μm, and 160 μm. However, for our analysis when we require to use high quality *AKARI* data with FQUAL = 3 only 51 of these 332 AGN have high quality data in three *AKARI* bands. Therefore we use additional far-IR data when available as described in section 3.

Swift/BAT Spectroscopic Survey (BASS; Koss et al. 2017) DR1 release provides multiwavelength data of 836 local AGN from the *Swift*-BAT 70-month catalogue (Baumgartner et al. 2013). The broad-band X-ray (between 0.3–150 keV range) spectral analysis of the BASS AGN sample is completed by Ricci et al. (2017a). They combine *Swift*-XRT, *XMM-Newton*, *ASCA*, *Chandra*, and *Suzaku* observations for the soft X-ray (0.3–10 keV) spectral analysis. They fit the AGN continuum with a simple power-law model with Galactic absorption and use different models (see their table 2) when necessary to improve the fit. In order to measure the column density along the line-of-sight Ricci et al. (2017a) take into account both photoelectric and Compton scattering with ZPHABS and CABS models, respectively. BASS includes 311 of the AGN in our *AKARI* AGN sample, therefore for these sources we adopt the N_H values from BASS; except ESO244-IG030 and ESO317-G041 for which we adopt the revised N_H measurements from Marchesi et al. (2019). For 19 AGN in our *AKARI* AGN sample we take the published N_H values from the literature (Maiolino et al. 1998; Fukazawa et al. 2001; Pappa et al. 2002; Zhang et al. 2006; Shu et al. 2007; Malizia et al. 2007, 2008, 2011, 2012; Pian et al. 2010; de Rosa et al. 2012; Matt et al. 2012; Baloković et al. 2014; Gandhi et al. 2015, 2017; Koss et al. 2016; Giustini et al. 2017; She et al. 2017; Iwasawa et al. 2018; Marchesi et al. 2019), based on the soft X-ray spectral analysis. We take X-ray data of 8 sources from public archives and perform the X-ray data analysis as described in Appendix A. In total 338 AGN in our sample have N_H measurements.

We focus our study on the hard X-ray selected *AKARI*-BAT AGN sample that includes 338 sources with measured N_H values. A flow-chart describing the selection criteria of our final *AKARI*-BAT AGN sample is displayed in Fig. 1. We list several source properties in Table 1. Based on the listed N_H values in Table 1 our sample includes 133 unobscured, 153 obscured and 52 CT AGN. The redshift distribution of our sample of 338 AGN with reliable spectroscopic redshift measurements is shown in Figure 2. The median redshift of our sample is 0.02.

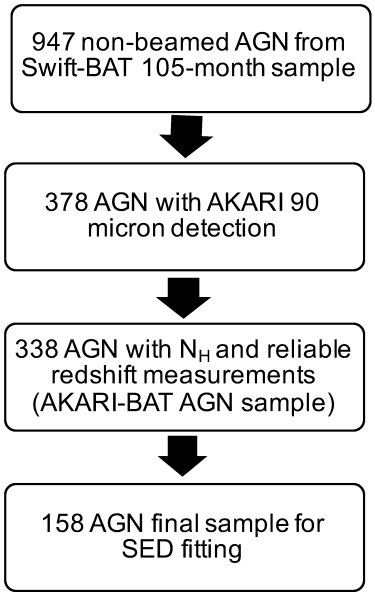

Figure 1. Flow-chart with all applied selection criteria for our *AKARI*-BAT AGN sample.

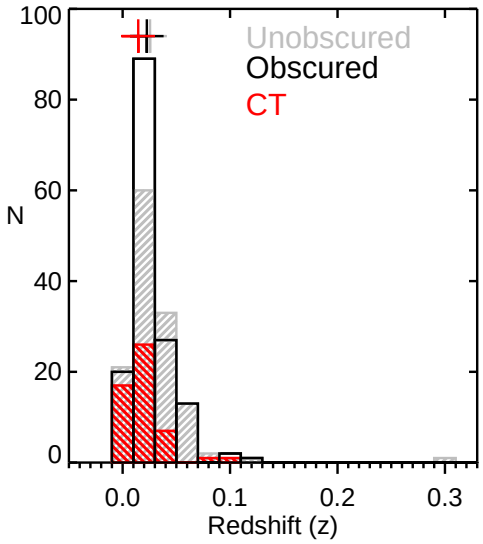

Figure 2. Redshift distribution of 338 hard X-ray selected *AKARI* AGN sample. The median redshift of our sample is 0.023. The median redshifts (shown by the plus signs) of the unobscured, obscured and the CT AGN are 0.025, 0.023 and 0.014, respectively. For visual inspection the distribution is shown up to z = 0.33, there are only two sources beyond this limit at z = 0.51 and z = 0.60.

Table 1. Hard X-ray selected *AKARI* AGN sample. The full table is available in the electronic version of the article. Columns: (1) *Swift* ID from *Swift*-BAT 105-month survey catalogue. (2) *AKARI* ID from the *AKARI*/FIS all-sky survey bright source catalogue version 2. (3) and (4) Optical counterpart coordinates from *Swift*-BAT 105-month survey catalogue. (5) Redshift of the optical counterpart from *Swift*-BAT 105-month survey catalogue. (6) Base 10 logarithm of the intrinsic Hydrogen column density in units of cm^{-2}. (7) X-ray spectral analysis reference for the adopted $\log(N_{\rm H})$ measurement. (8) Base 10 logarithm of the pure AGN luminosity in the IR band measured from the SED fitting by CIGALE. (9) The fractional AGN emission contribution to the total IR luminosity. (10) The 14–195 keV luminosity adopted from *Swift*-BAT 105-month survey catalogue. (11) *WISE* 22 μm ($W4$) magnitude. (12) – (15) The *AKARI* 9, 18, 65, 90 μm magnitudes from the *AKARI*/FIS all-sky survey bright source catalogue version 2. and *AKARI*/IRC all-sky survey point source catalogue version 1.

Swift source name (1)	*AKARI* source name (2)	RA (J2000.0) (deg) (3)	Dec (J2000.0) (deg) (4)	z (5)	$\log(N_{\rm H})$ (6)	X-ray Ref. (7)	$\log(L(IR)_{AGN}$ / erg s^{-}) (8)	$frac_{\rm AGN}$ (9)	$\log(L_{14-195}$ / erg s^{-}) (10)	$F(22)$ μm) (AB) (11)	$F(9)$ μm) (AB) (12)	$F(18)$ μm) (AB) (13)	$F(65)$ μm) (AB) (14)	$F(90)$ μm) (AB) (15)
J0002.5+0323	0002261+032111	0.6103	3.3519	0.0255	$20.0^{0.0}_{0.0}$	Bass Survey	···	···	43.20	11.39 ± 0.03	···	···	8.91 ± 0.27	9.08 ±0.06
J0006.2+2012	0006196+201211	1.5813	20.2029	0.0258	$20.5^{0.0}_{0.2}$	Bass Survey	44.66	0.6	43.38	10.19 ± 0.02	11.13 ± 0.03	10.53 ± 0.20	9.35 ±0.34	10.17 ± 0.17
J0038.4+2337	0038319+233652	9.6339	23.6133	0.0249	$23.0^{0.1}_{0.1}$	Bass Survey	···	···	43.26	12.10 ± 0.04	···	···	11.37 ± 1.18	10.04 ± 0.14
J0042.9-2332	0042531-233224	10.7200	-23.5410	0.0222	$23.5^{0.1}_{0.1}$	Bass Survey	43.72	0.3	43.77	9.95 ± 0.02	···	10.23 ± 0.11	8.08 ± 0.21	8.75 ± 0.07
J0042.9+3016A	0043022+301721	10.7578	30.2888	0.0520	$22.3^{0.1}_{0.2}$	Bass Survey	···	···	43.60	11.32 ± 0.03	···	···	10.82 ± 0.95	10.00 ± 0.14
J0051.6+2928	0051348+292408	12.8959	29.4013	0.0360	$20.0^{0.0}_{0.0}$	Bass Survey	44.24	0.1	43.49	11.41 ± 0.03	···	···	10.03 ± 0.61	8.74 ±0.05
J0105.5-4213	0105260-421256	16.3617	-42.2162	0.0302	$24.2^{0.1}_{0.2}$	Bass Survey	···	···	43.48	10.94 ± 0.02	···	11.39 ± 0.26	9.42 ± 0.40	10.17 ± 0.15

3 DATA

To gain insight into the nature of our hard X-ray selected *AKARI*-BAT AGN sample by investigating their spectral energy distributions (§4) and colours (§5.3 and §5.4) we collect archival photometry from UV to far-IR.

Galaxy Evolution Explorer (*GALEX* Martin et al. 2005) performed a comprehensive sky survey at near-UV (NUV) and far-UV (FUV) bands at $\lambda_{\rm eff}$ = 2267Å and $\lambda_{\rm eff}$ = 1516Å, respectively. The revised catalog of *GALEX* ultraviolet sources (Bianchi et al. 2017) lists revised photometric measurements and eliminates any duplicate entries. We cross match optical counterpart positions of AGN in our sample with the revised catalog of *GALEX* ultraviolet sources within a separation threshold of 5 arcsec and find 205 UV counterparts. Since Bianchi et al. (2017) only include sources from All-Sky Imaging Survey (AIS) observations with both FUV and NUV detectors exposed, their catalogue do not include sources exposed only with a single FUV or NUV detector. To include such sources in our UV counterpart sample, the remaining 173 sources were cross matched (using a search radius of 5 arcsec) with GALEX source catalogue (Martin et al. 2005) Data Release 6 (DR6) from MAST Portal[2]. After dropping matches with measurements with dichroic reflections (NUV_ARTIFACT = 4) and keeping only the single photometric measurement with the longest duration for multiple observations of the same source, we find 56 more *GALEX* counterparts. In total we find 261 *GALEX* counterparts. We correct the UV photometric measurements for Galactic foreground extinction using the listed E_{B-V} values (based on the extinction maps of Schlegel et al. 1998) in the *GALEX* catalogues.

For the optical counterparts we extract the Galactic extinction corrected *u*-, *g*-, *r*-, *i*-, *z*-band magnitudes from the Sloan Digital Sky Survey (SDSS; York et al. 2000) Data Release 14 (Abolfathi et al. 2018) *PhotoObjAll* catalog [3]. We find only 146 sources in the SDSS DR 14 footprint. However 67 galaxies whose photometric flags include CLEAN = 0 are not reliable and therefore not included in our analysis. We visually inspected images of the remaining galaxies and discarded any suspicious photometry of: (i) very large (nearby) galaxies whose automated deblending is unreliable; (ii) too bright galaxies close to the r-band saturation magnitude limit at r = 14.5 (Strauss et al. 2002); (iii) galaxies with contaminated by superposed stars. We use near-infrared Two Micron All Sky Survey (2MASS; Skrutskie et al. 2006) *J*-, *H*-, K_s-band magnitudes from the Two Micron All Sky Survey Extended Source Catalog (2MASS XSC; Jarrett et al. 2000) and 2MASS Point Source Catalog (Cutri et al. 2003). For the 332 sources in the 2MASS XSC we use the '20mag/sq.' isophotal fiducial elliptical aperture magnitudes. For the 17 sources in the 2MASS Point Source Catalog we use default magnitudes. We check photometry artifact contamination and/or confusion flag (cc_flag) and use only realiable measurements. 2MASS magnitudes were corrected for Galactic extinction based on the Schlegel et al. (1998) maps and the extinction law of Cardelli et al. (1989).

In order to include *AKARI* and *WISE* mid-IR photometry at 3.4, 4.6, 9, 12, 18 and 22 μm, we cross-match *AKARI*/FIS coordinates of our hard X-ray selected *AKARI* AGN sample with the *AKARI*/IRC all-sky survey point source catalogue version 1[4] and the AllWISE source catalogue[5] (Cutri et al. 2013) using a search radius of 20 arcsec.

Herschel Space Observatory (*Herschel*; Pilbratt et al. 2010) mapped about a small fraction of the sky in far-infrared and sub-millimeter bands centred at 70, 100, 160, 250, 350 and 500 μm with the Photodetector Array Camera and Spectrometer (PACS; Poglitsch et al. 2010) and Spectral and Photometric Receiver (SPIRE; Griffin et al. 2010) instruments. Meléndez et al. (2014) and Shimizu et al. (2016) present *Herschel* PACS and SPIRE photometric measurements for 313 AGN from the 58 month *Swift*/BAT catalog (Baumgartner et al. 2013), respectively. By matching the optical counterpart names with *Herschel*-BAT AGN sample of Meléndez et al. (2014) and Shimizu et al. (2016) we find *Herschel* PACS photometry for 155 and SPIRE photometry for 187 AGN in our sample.

When photometric fluxes from *AKARI*, *WISE* and *Herschel* are combined for the SED analysis (§4) the spatial resolution differences among each band may cause nuclear and host galaxy IR emission measurement discrepancies (e.g. Clements et al. 2019). The beam size for the *AKARI*/FIS is (beam FWHM is ~ 30−50 arcsec, Doi et al. 2015) larger than that of *Herschel*/PACS (beam FWHM is ~ 6 − 11 arcsec, Poglitsch et al. 2010). As shown by Clements et al. (2019) when *AKARI* FIR fluxes are compared to *IRAS* fluxes, the ~ 10 times better angular resolution of *AKARI* causes missing FIR emission for extended sources. Clements et al. (2019) derive beam corrections that should be applied to *AKARI*/FIS all-sky survey bright source catalogue version 2 fluxes at 65μm and 90 μm. These corrections depend on the extendedness parameter measured as the *J* band magnitude difference between the 2MASS point source catalogue and 2MASSX extended source catalogue. We apply this beam correction (see equation 2 of Clements et al. 2019) to the 65μm and 90μm *AKARI*/FIS fluxes in our sample. The applied beam correction results an average of 4% and 20% additional flux at 65μm and 90μm, respectively. Clements et al. (2019) also find that no beam corrections are needed for the moderately extended sources at 140μm and 160μm bands.

As reported by Mushotzky et al. (2014) bulk of BAT sources are point like with a compact host galaxy with *Herschel* spatial resolution. The comparison of aperture correction applied (as described in the above) *AKARI*/FIS 65μm (S_{65}^{AKARI}) and *Herschel*/PACS 70μm (S_{70}^{PACS}) fluxes for 61 sources in our sample show a a good agreement (Fig. 3), the median difference between the two fluxes is 18 per cent with respect to S_{65}^{AKARI}. A typical difference of 18 per cent between the two fluxes is added in the quadrature to the flux uncertainties of the S_{65}^{AKARI} fluxes. Since both S_{70}^{PACS} and S_{65}^{AKARI} fluxes agree, we use both as independent photometric measurements in our SED analysis. 30 sources in our sample have both high quality *AKARI*

[2] http://mast.stsci.edu
[3] https://skyserver.sdss.org/dr14/
[4] http://www.ir.isas.jaxa.jp/AKARI/Observation/PSC/Public/RN/AKARI-IRC_PSC_V1_RN.pdf
[5] http://wise2.ipac.caltech.edu/docs/release/allwise/

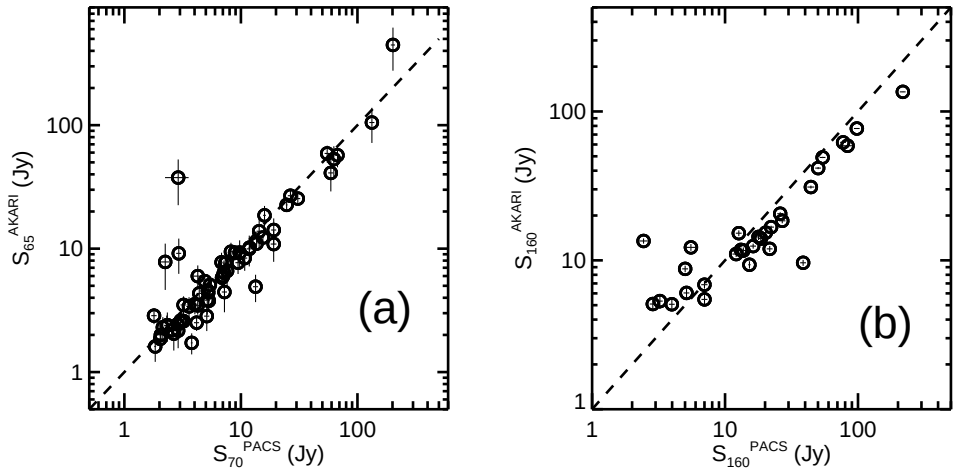

Figure 3. Comparison between the PACS and *AKARI* fluxes at 70 μm–65 μm (a) and 160 μm–160 μm (b). The dashed lines represent $y = x$.

and PACs fluxes at 160 μm band. As shown in Fig. 3, the median percentage difference between *AKARI* and PACS 160 μm fluxes is 32% with respect to the *AKARI* fluxes. As reported by Mushotzky et al. (2014) the FIR radiation of the most BAT sources are point-like at the spatial resolution of *Herschel*. Additionally, Meléndez et al. (2014) and Shimizu et al. (2016) present PACs measurements for an appropriate aperture for each source, therefore we prefer to use PACs 160 μm fluxes for these 30 AGN. If *Herschel*/PACs 160 μm band photometry is not available we use AKARI/FIS 160 μm flux measurements for the rest of our sample. Since both *AKARI*/FIS 140 μm and 160 μm bands are similar, to be conservative we add a 32% flux uncertainty in the quadrature to the photometric uncertainties of the 140 μm and 160 μm fluxes.

The 9 arcsec beam size of *AKARI*/IRC is (Ishihara et al. 2010) similar to the beam size of *WISE* that is between 6 arcsec and 12 arcsec (Wright et al. 2010). We only use *WISE* measurements with zero *cc_flags* values (*cc_flags* =′ 0000′) to avoid contaminated measurements (i.e., by diffraction spikes, bright sources). For extended *WISE* sources (with *ext_flg* > 0) we use elliptical aperture magnitudes (‘*wngmag*’, *n* is the band number). For *AKARI*/IRC photometry we only include measurements with high quality (*FQUAL*(9 μm) = 3, *FQUAL*(18 μm) = 3). *AKARI*/IRC 9 μm, 18 μm and *WISE* 12 μm, 22 μm bands have close but slightly different central wavelengths. In our sample 112 sources have both *AKARI*/IRC 9 μm and *WISE* 12 μm fluxes. Additionally, 139 sources have both *AKARI*/IRC 18 μm and *WISE* 22 μm measurements. For these sources, the comparison of *AKARI*/IRC and *WISE* fluxes agree (the mean percentage difference ∼20%) without any systematic differences. Therefore, we do not apply any aperture correction at these bands and use each photometric measurement separately in our SED analysis. However, to be conservative we add the typical flux difference of ∼20% in the quadrature to the photometric uncertainties of the 9 μm, 12 μm, 18 μm and 22 μm fluxes.

4 INFRARED SPECTRAL ENERGY DISTRIBUTIONS OF UNOBSCURED OBSCURED AND COMPTON-THICK AGN

We perform SED fitting based on the collected photometric data by using the Code for Investigating Galaxy Emission (CIGALE; Noll et al. 2009; Serra et al. 2011; Boquien et al. 2019) version 2018.0. CIGALE[6] is a modern galaxy SED modelling code that applies energy conservation principle between the near-infrared/optical/ultraviolet emission that is absorbed by dust and the re-emitted mid-infrared and far-infrared emission. CIGALE models host galaxy emission and AGN component separately. CIGALE combines several built models based on the given input parameters for stellar, dust and AGN components. As a result it generates the probability distribution function of the model parameters. The mean value of the probability distribution function is the output value of a parameter. The standard deviation measured from the probability distribution function is the associated error of the parameter.

Stellar component models include the stellar population, Initial Mass function (IMF) and star formation history. Here we adopt the stellar population models of Maraston (2005) with Salpeter IMF (Salpeter 1955) and a double exponential star formation history. For the dust component we use the dust models of Draine et al. (2014) and for the dust attenuation we use modified Charlot & Fall (2000) attenuation law. We model the AGN component with the models from Fritz et al. (2006). These AGN models are composed of the isotropic central source emission in the form of power laws between 0.001–20μm and the dust emission of the toroidal obscurer. In these models the central AGN emission can be partly absorbed by the dust and re-emitted at 1-1000μm or scattered by the dust. In Table 2 we list the adopted parameters used for the SED fitting. Table 2 includes 17 parameters, but we note that some of the parameters and data are correlated and interconnected. As a result, the number of degrees of freedom is not 17. CIGALE

[6] http://cigale.lam.fr/.

compares one dataset (with N observed data points) to every single model. So the Bayesian method used in CIGALE do not estimate each parameter separately but measure the likelihood of each model (built from a set of parameters) to match the dataset. And from these likelihoods, the probability are evaluated and the probability distribution functions are built.

In CIGALE the quality of the parameter estimation process depends on the provided data points at different regions over the SED. For example, CIGALE uses UV-optical and near-infrared data to model stellar component. Additionally mid-infrared and far-infrared data are needed to model the dust component. To estimate reliable luminosities from the SED fitting, we require to have at least one detection at each UV-optical, near-infrared, mid-infrared and far-infrared regions. For the far-infrared part, to accurately constrain the dust SED we require to have at least one detection at shorter wavelengths than the peak of the dust SED near 100μm and at least one detection at longer wavelengths. Table 3 list the broad-band filters included in our SEDs, the detection rate of our sample of 338 AGN at each band and the number of sources detected at different wavelength regions of the SED. The data requirement for the SEDs ensures all of the SEDs to have at least 5 data points. As a result of the applied wavelength coverage criteria we perform SED fitting analysis for 158 AGN in our sample. Among those 68 are unobscured, 65 are obscured and 25 are CT AGN.

Fritz et al. (2006) model the AGN emission by considering the radiative transfer model of three main emission components. These are: (i) the central illuminating source; (ii) the scattered emission by dust in the torus; (iii) the thermal dust emission from the torus. These models depend on seven parameters. The size of the torus, r is defined by ratio of the maximum outer radius to minimum innermost radius of the dust torus. According to the model, $r_$ratio can have the values of 10, 30, 60, 100 and 150. The main dust components are silicate and graphite grains. Silicate grains are responsible for the absorption feature at 9.7 μm, and τ is the optical depth at 9.7 μm. In these models τ can be 0.1, 0.3, 0.6, 1.0, 2.0, 3.0, 6.0 and 10.0. The dust density distribution is determined by $r^{\beta}e^{-\gamma|cos\theta|}$. Here, the β parameter is related to the radial dust distribution in the torus and can have the values of -1.00, -0.75, -0.50, -0.25 and 0.00. The γ parameter is related to the angular dust distribution in the torus and may have the values of 0.0, 2.0, 4.0 and 6.0. θ is the opening angle of the torus, it can have the values of 60°, 100° or 140°. The angle between equatorial axis and line of sight, ψ, can have values between 0.001 and 89.990 in steps of 10 degrees. ψ = 90° for Type 1 AGN and ψ = 0° for Type 2 AGN.

In this work, our main interest is to constrain the parameters of the AGN component and measure the AGN and dust luminosities. We obtain statistically good fits ($\chi^2_{reduced} \leq 5.0$) for most sources except four unobscured AGN (M81, NGC4579, NGC4235, NGC5273). We show examples of SED fitting for one CT and one obscured AGN with good photometric coverage from UV to FIR including optical and near-IR bands, in Figure 4.

We obtain several physical quantities as a result of the SED analysis by CIAGLE. These are: (i) the host galaxy dust luminosity, $L_{\rm dust}$, is measured from the best-fitted dust emission model (the red component in Fig. 4) from the models of Draine et al. (2014); (ii) the pure AGN luminosity in the IR band, $L(\rm IR)_{\rm AGN}$ based on the Fritz et al. (2006) AGN model (the green component in Fig. 4); $L(\rm IR)_{\rm AGN}$ is the sum of three AGN luminosity components (the direct emission from the central engine, the thermal emission from torus and the scattered emission from the torus); (iii) the total IR luminosity $L(\rm IR)_{\rm TOTAL}$ can be measured as the sum of $L_{\rm dust}$ and $L(\rm IR)_{\rm AGN}$. The physical origin of $L_{\rm dust}$ is the host galaxy dust grains heated by the interstellar radiation (Draine et al. 2014).

Based on the analysis of the 68 unobscured, 65 obscured and 25 CT AGN SEDs we find that the fractional AGN emission contribution to the total IR luminosity ($frac_{\rm AGN}$) is between 10 and 80%. Based on the $frac_{\rm AGN}$ values listed in Table 1 we identify 7 unobscured, 2 obscured and 18 CT AGN with high ($\geq$ 40%) AGN contribution to the total infrared luminosity. These sources represent IR SEDs with strong AGN luminosity and weak star formation activity from the host galaxy. We have also checked if there is a correlation between the $frac_{\rm AGN}$ value and the $\rm N_H$. We find that while unobscured and obscured AGN have a similar $frac_{\rm AGN}$ distribution between 10 and 60%, CT AGN have higher $frac_{\rm AGN}$ values within the 10 and 80% range. Unobscured and obscured AGN do not show a correlation between $frac_{\rm AGN}$ and $\rm N_H$. On the other hand, CT-AGN tend to have higher $frac_{\rm AGN}$.

As a result of the SED analysis of 68 unobscured, 65 obscured and 25 CT AGN we find that while unobscured AGN can have ψ values between 30.10° and 89.990°, all obscured and CT AGN have ψ values of 0.001°or 20.0° as expected. Our analysis confirm that the angle between equatorial axis and line of sight an important parameter to separate obscured and unobscured AGN based on the SED fitting using this model. We find that CT and obscured AGN have θ values of 140° (52 per cent), 100° (32 per cent) or 60° (15 per cent). Unobscured AGN can have θ values of 140° (53 per cent), 100° (32 per cent) or 60° (14 per cent). We find that unobscured, obscured and CT AGN mostly have β = −0.5 or β = −1.00. Unobscured, obscured and CT AGN mostly have γ = 4.0 and γ = 6.0. Models with r_ratio equal to 150 are favoured for unobscured, obscured and CT AGN. Models with τ equal to 10.0 provide good fits for the most of the unobscured, obscured and CT AGN.

Our SED analysis with CIGALE shows that obscured and CT AGN can be identified based on the parameters of the Fritz et al. (2006) model, the most critical parameters are the angle between equatorial axis and line of sight ψ, angular opening angle of the torus, θ . Once the best fitted SED given by CIGALE has ψ = 0.001° or ψ = 10.0°, and θ = 140°, then it is very likely that the source is an obscured/CT AGN.

5 RESULTS AND DISCUSSION

5.1 Average SEDs of Unobscured Obscured and Compton-thick AGN

As a result of our SED analysis across the UV to far-IR wavelength region, we make average SEDs of unobscured, obscured and CT AGN. We build the mean best-fitted SEDs by CIGALE as follows: (i) the fluxes densities at each frequency

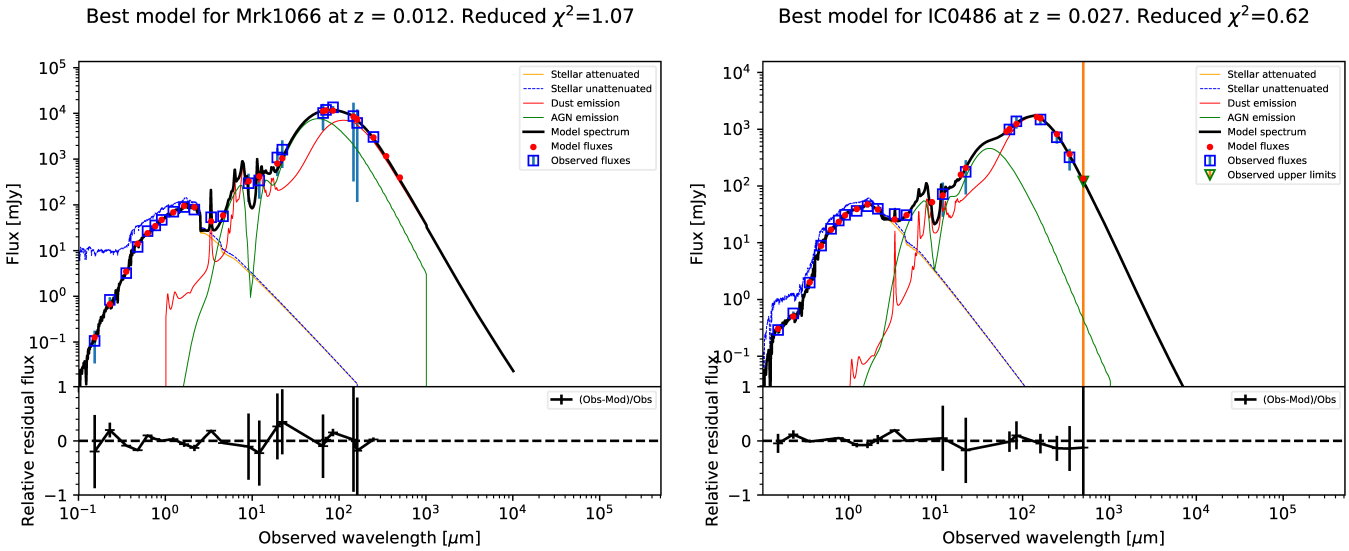

Figure 4. Examples of best-fitting models of one CT (left) and one obscured (right) AGN obtained with CIGALE. These SEDs are representative of SEDs with full photometric coverage data from UV to FIR. Blue squares are the measured flux densities (from *GALEX*, SDSS, 2MASS, *WISE*, *AKARI* and *Herschel*) of the AGN. Filled circles (red) are best-fitting model fluxes. The black solid lines are the best fits given by CIGALE. The dashed blue lines, the solid red lines and the solid green lines show the unattenuated stellar emission, the dust emission and the total AGN emission, respectively.

Table 2. Parameters used in the SED fitting by CIGALE.

Parameter	Value
	SFH
Main stellar age	200,300,400,500,600,700,800,900,1000, 2000,2600,2900,3000,3500,4000,5000,10000
burst age	1,2,6,10, 20,30,40,50,80,90,100,150,200,380,400,450,600,900,950,1400
τ_{main}	20,100,200,500,1000,1200,1300,3000,6000,7000
τ_{burst}	1,5,10, 50
	Dust emission
q_{PAH}	0.47, 1.12, 1.77, 2.50
U_{min}	0.170, 0.200, 0.250, 0.350, 0.500, 0.600, 0.700,1.000, 1.200, 1.500, 1.700, 2.000, 2.500, 3.000, 3.500, 4.000, 5.000, 6.000, 7.000, 8.000, 10.00, 12.00
α	1.7, 1.8, 1.9, 2.0, 2.1, 2.2, 2.3, 2.4, 2.6, 2.7, 2.8, 2.9, 3.0
γ	0.02, 0.1, 0.2, 0.3, 0.4
	Dust attenuation
slope ISM	-0.7,-0.5,-0.3,-0.1
slope birth clouds	-1.3, -0.7
	AGN
R_{max}/R_{min}	10, 30, 60, 100, 150
τ	0.1, 0.3, 0.6, 1.0, 2.0, 3.0, 6.0, 10.0.
β	-1.00, -0.75, -0.50, -0.25, 0.00
γ	0.0, 2.0, 4.0, 6.0
θ	60, 100, 140
ψ	0.001, 10.100
$frac_{AGN}$	0.1, 0.2, 0.3, 0.4, 0.5, 0.6, 0.7

are converted to luminosity; (ii) we calculate the mean SED at each $\log\nu$ grid point ($\Delta\log\nu = 0.0007$), we normalise each SED at 1μm. Fig. 5 shows the mean SEDs of unobscured, obscured and CT AGN in panels (a), (b) and (c), respectively. Panel (d) shows the mean SEDs of each population together. As seen in panel (d) in the optical-UV region, unobscured AGN have strong contribution compared to the obscured/CT AGN. This is consistent with the adopted AGN model of Fritz et al. (2006) since the emission from the inner the torus is completely absorbed due to the optically thick torus. Therefore, the mean SEDs of the obscured/CT AGN dominated by the stellar population emission in the optical-

Table 3. Photometric filters used in the SEDs and the detection rate out of 338 AGN in our sample at each band. Columns: (1) Telescope/survey name. (2) Filter name. (3) Efficient wavelength of the filter. (4) Number of detections of the 338 AGN in our sample at each band. (5) Number of sources that has at least one detection at each region: region A is UV-optical (covers FUV, NUV,u,g,r,i,z bands), B is NIR (covers J, H,Ks bands), C is MIR (covers w1,w2,w3,w4,S9W,L18W bands) and D is FIR (covers N60,WIDE-S,WIDE-L,N160,PACS blue,PACS red bands). Each region is separated by the horizontal lines.

Telescope/ Survey	Filter	$\lambda_{\rm eff}(\mu{\rm m})$	Detection rate at each band	Number of sources at least one detection in each region
GALEX	FUV	0.15	173	
	NUV	0.23	222	
SDSS	u	0.36	75	
	g	0.46	75	A= 244
	r	0.61	75	
	i	0.74	75	
	z	0.89	75	
2MASS	J	1.24	335	
	H	1.66	335	B=335
	Ks	2.16	335	
WISE	w1	2.25	256	
	w2	4.60	256	
	w3	11.56	255	
	w4	22.09	255	C=305
AKARI	S9W	9	149	
	L18W	18	186	
AKARI	N60	65	92	
	WIDE-S	90	333	
	WIDE-L	140	120	
	N160	160	23	D=338
Herschel	PACS blue	68.927	155	
	PACS red	153.95	155	
Herschel	PSW	242.82	187	
	PMW	340.89	187	
	PLW	482.25	187	

UV region. Near rest frame 10μm the mean AGN continuum is slightly stronger for unobscured AGN compared to the that of obscured/CT AGN. This can be understood as a result of the relatively stronger silicate absorption feature seen in the obscured/CT AGN. The mean SEDs are very similar in between the 1 - 20μm mid-IR range. The obtained mean SED properties of obscured, unobscured and CT AGN in the optical to mid-IR range agree with previously obtained composite SEDs of Type 1 and Type 2 (e.g., Hickox et al. 2017). In the MIR region PAH emission from host-galaxy star-light is stronger in the mean SED of the CT AGN. The mean SED of the CT AGN shows a stronger FIR bump compared to the un/obscured mean SEDs. This is consistent with the more FIR emission observed in type-2 quasars (e.g., Hiner et al. 2009; Chen et al. 2015). The far-IR emission is expected to be formed by the cold-dust emission heated by star formation. However, as suggested by Hiner et al. (2009) dust heated by AGN can have a significant contribution to the far-IR emission. The stronger FIR emission of CT AGN supports a connection between the AGN obscuration and host galaxy dust emission.

5.2 Relations Between the Infrared Luminosities and Ultra Hard X-ray Luminosity

As a result of the SED fitting analysis in §4, we measure the dust luminosity, $L_{\rm dust}$, the pure AGN luminosity in the IR band, $L({\rm IR})_{\rm AGN}$ and the total IR luminosity $L({\rm IR})_{\rm TOTAL}$ as the sum of the $L_{\rm dust}$ and $L({\rm IR})_{\rm AGN}$. Here we quantify the relationships between $L_{\rm dust}$, $L({\rm IR})_{\rm AGN}$, $L({\rm IR})_{\rm TOTAL}$ and the ultra hard X-ray luminosity in the 14-195 keV band. Figure 6 shows the relations between $L_{\rm dust}$, $L({\rm IR})_{\rm AGN}$, $L({\rm IR})_{\rm TOTAL}$ and L_{14-195} for unobscured, obscured and CT AGN in our sample. Clear, positive correlations are seen for $L_{\rm dust}$-L_{14-195} (left panel), $L({\rm IR})_{\rm AGN}$-L_{14-195} (middle panel) and $L({\rm IR})_{\rm AGN}$-L_{14-195} (right panel). We determine the significance of the correlations using Pearson correlation coefficient (r, Pearson 1896). We measure $\sim r = 0.6$ with a p-value equal to zero which indicates a moderately strong correlation for all luminosities.

To characterise the L_{dust}-L_{14-195}, $L({\rm IR})_{\rm AGN}$-L_{14-195} and $L({\rm IR})_{\rm TOTAL}$-L_{14-195} relationships, we adopt the following parameterisation:

$$\log(L_{dust}) = A_{dust} + \alpha_{dust}\log(L_{14-195}) + \epsilon_{dust}. \quad (1)$$

$$\log(L({\rm IR})_{\rm AGN}) = {\rm A}_{\rm AGN} + \alpha_{\rm AGN}\log({\rm L}_{14-195}) + \epsilon_{\rm AGN}. \quad (2)$$

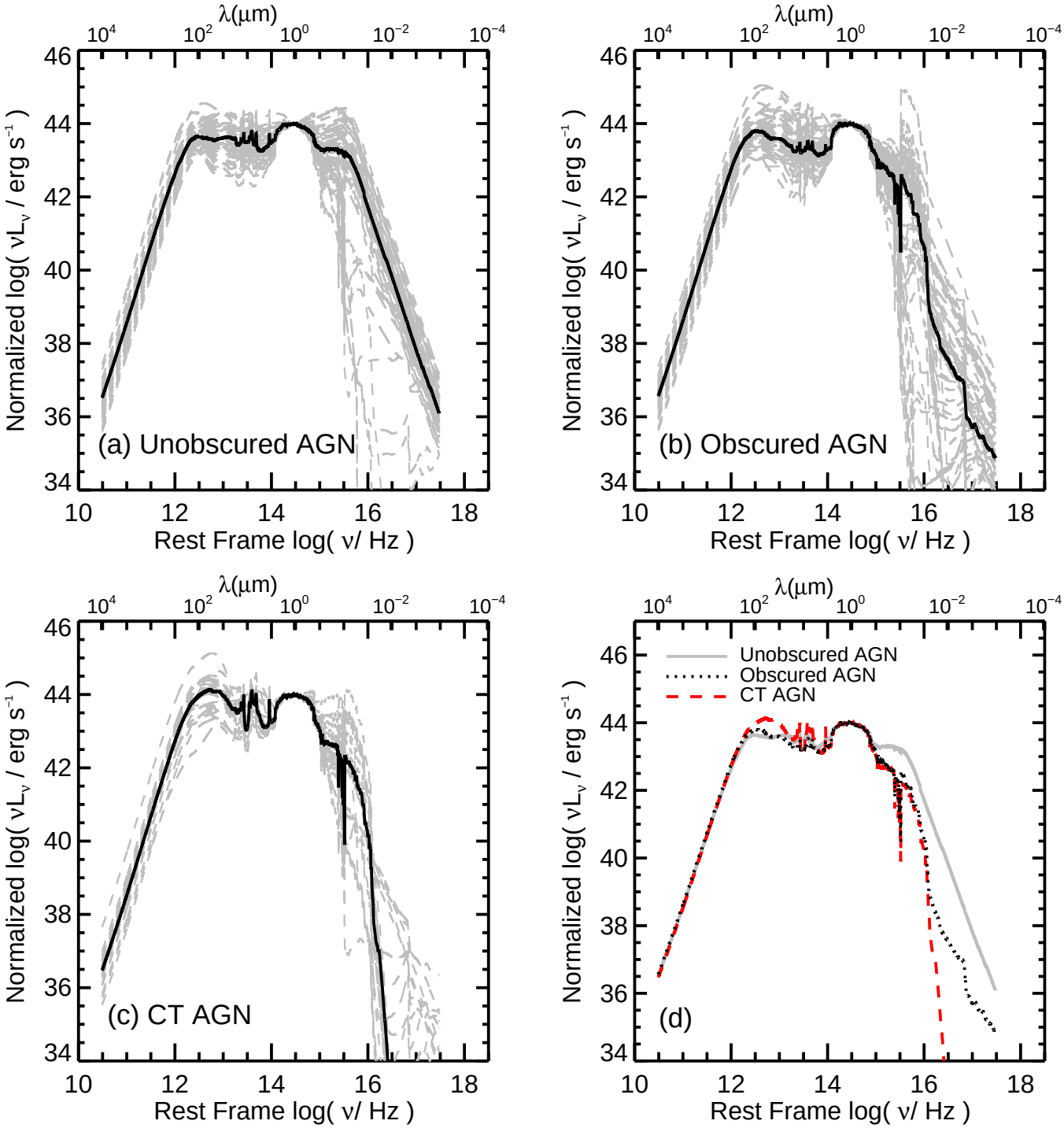

Figure 5. Obtained mean SEDs of unobscured (panel a), obscured (panel b) and CT (panel c) AGN populations as a result of SED analysis by CIGALE. In panel (d) the mean SEDs are shown on top of each other. All SEDs are normalised at rest frame 1μm.

$$\log(L(\mathrm{IR})_{\mathrm{TOTAL}}) = \mathrm{A}_{\mathrm{TOTAL}} + \alpha_{\mathrm{TOTAL}} \log(\mathrm{L}_{14-195}) + \epsilon_{\mathrm{TOTAL}}. \quad (3)$$

where A is the zero point, α is the slope and ϵ is the estimated scatter. We establish the best-fitting relationships for both luminosities by the Bayesian regression method of (Kelly 2007) that accounts for scatter (ϵ) and computes the posterior probability distributions of the parameters.

For the L_{dust}-L_{14-195} relationship the best-fitting parameters are: A_{dust}= 22.08±3.27, α_{dust}= 0.51±0.07 and ϵ_{dust}= 0.43±0.03. The best-fitting relationship for all sources is shown as the solid line. The dashed line, which is very similar to the solid line, shows the best-fitting relationship of obscured and CT AGN. Best-fitting parameters for $L(\mathrm{IR})_{\mathrm{AGN}}$-$L_{14-195}$ relationship are: A_{AGN}= 15.50±2.91,

α_{AGN}= 0.66±0.07 and ϵ_{AGN}= 0.53±0.03. The best-fitting relationship is shown as the solid black line for the unobscured, obscured and CT AGN. When we only consider the obscured and CT AGN we find a slightly shallower slope of α_{AGN}= 0.58±0.10 as shown by the dashed black line. Best-fitting parameters for $L(\mathrm{IR})_{\mathrm{TOTAL}}$-$L_{14-195}$ relationship are: A_{TOTAL}= 19.35±2.23, α_{TOTAL}= 0.57±0.05 and ϵ_{TOTAL}= 0.40±0.02. The best-fitting relationship (dashed line) for obscured and CT AGN is slightly shallower than that of the all sources (solid line). The slope of the dashed line is α_{TOTAL}= 0.52±0.08. The obtained scatter values around the best-fitting relationships are similar (between 0.4 and 0.5) for all panels. The L_{dust}-L_{14-195} relationship slope is shallower compared to that of $L(\mathrm{IR})_{\mathrm{AGN}}$-$L_{14-195}$. Since $L(\mathrm{IR})_{\mathrm{AGN}}$ is the pure AGN luminosity and L_{dust} originates from starburst radiation we expect to have different slopes for these relationships.

The relationship between the AGN mid-IR luminosity and X-ray luminosity has been investigated by previous studies (e.g., Asmus et al. 2015; Ichikawa et al. 2017, 2019). Ichikawa et al. (2019) decomposed the IR SED of the 587 AGN in the 70-month *Swift*/BAT sample into starburst and AGN components. They quantified the relationship between the 12μm, mid-IR luminosities and the ultra hard X-ray luminosity in the 14-195 keV for *Swift*/BAT 70-month AGN. When we compare the $L(\mathrm{IR})_{\mathrm{AGN}}$-$L_{14-195}$ relationship slope with the mid-IR AGN luminosity L_{14-195} relationship slope values between 0.96-1.06 obtained by Asmus et al. (2015); Ichikawa et al. (2017, 2019), we obtain a much shallower slope. The obtained shallower slope in this work might be related to the sample difference. First of all our AGN sample (158) is much smaller compared to that of Ichikawa et al. (2017, 2019) and therefore it does not expand to low and high luminosity ranges in both axis. Especially, our sample do not have any AGN with $\log L_{14-195} > 45.0$ and $L(\mathrm{IR})_{\mathrm{AGN}} < 41.5$, therefore we obtain a shallower slope compared to other studies (e.g., Asmus et al. 2015; Ichikawa et al. 2017, 2019) whose samples include higher L_{14-195} and lower $L(\mathrm{IR})_{\mathrm{AGN}}$ objects. An other difference that may result in different slope values is the difference between the measured IR luminosities, while we have the AGN luminosity in the total IR range previous works (e.g., Asmus et al. 2015; Ichikawa et al. 2017, 2019) only consider the mid-IR luminosity. We also note that, slope values of ~0.65 (e.g. Netzer 2009; Matsuoka & Woo 2015) and ~ 0.8 (Ichikawa et al. 2017) are obtained for the relationship between the far-IR luminosity and the bolometric AGN luminosity. The obtained α_{dust}= 0.51±0.07 slope in this work is close to the slope values obtained in these previous studies.

As shown in Figure 7 we also check the fraction of the pure AGN luminosity to the hard X-ray luminosity as a function $L(\mathrm{IR})_{\mathrm{AGN}}$ (left panel) and L_{14-195} (right panel). As seen in both panels, pure AGN luminosity to the hard X-ray luminosity fraction of obscured and CT AGN do not show a clear separation from the unobscured AGN.

The measured $L(\mathrm{IR})_{\mathrm{AGN}}$ as a result of the SED fitting can be used to calculate $R = L(\mathrm{IR})_{\mathrm{AGN}}/L(\mathrm{BOL})_{\mathrm{AGN}}$, which is a good indicator of dust covering factor (e.g. Elitzur 2012). For comparison we follow Ichikawa et al. (2019) and use a constant bolometric factor of 8.47 (Ricci et al. 2017b) to obtain $L(\mathrm{BOL})_{\mathrm{AGN}}$. In Figure 8 we show R versus $\mathrm{N_H}$ in order to see the differences of covering factors among unobscured, obscured and CT AGN. We find that the median covering factor of the CT AGN ($\log(R_{\mathrm{ct}})$=0.21) is larger than the median covering factor of the obscured ($\log(R_{\mathrm{obscured}})$=-0.71) and the median covering factor of the unobscured ($\log(R_{\mathrm{unobscured}}$=-0.34) AGN. For our sample we see that the median covering factor of the unobscured AGN is larger than that of the obscured AGN, however we note that the most majority of the obscured and unobscured AGN have R values in a similar range. For a larger sample of *Swift*/BAT AGN Ichikawa et al. (2019) found that obscured AGN have a larger covering factor compared to unobscured AGN. The found higher covering factor values of the CT AGN is consistent with the result of Ichikawa et al. (2019).

5.3 Infrared colours and luminosities versus $\mathrm{N_H}$

Here we investigate if the IR colours depend on the $\mathrm{N_H}$. Near-IR (NIR) photometry is a good tracer of direct-stellar component, the MIR photometry is a good tracer of AGN torus and the FIR photometry is a good tracer of host galaxy dust emission. Therefore, NIR-FIR and MIR-FIR colours have physically different origins. NIR-FIR colours represent the energy balance between the direct-stellar versus dust emission from the host galaxy, while the MIR-FIR colours give a comparison between the AGN torus versus host dust emission. We show the observed 1.25μm - 65 μm, 1.25μm - 90 μm, 18 μm - 65 μm, 18 μm - 90 μm, 22 μm - 65 μm, 22 μm - 90 μm colours versus $\mathrm{N_H}$ in Fig. 9. Since the median redshift of our sample is 0.02 we do not expect to have a significant redshift effect in the observed colours. As seen in Fig. 9 although there is a large scatter for individual colours, the median 1.25μm - 65 μm, 1.25μm - 90 μm, 18 μm - 65 μm, 18 μm - 90 μm, 22 μm - 65 μm, 22 μm - 90 μm, colours of the unobscured, obscured and CT AGN show an slightly increasing trend with $\mathrm{N_H}$. We note that we have checked other colour combinations and see a similar trend for H - 65 μm, H - 90 μm, K_s - 65 μm, K_s - 90 μm, 12 μm- 65 μm and 12 μm- 90 μm. This positive trend indicates that the MIR-FIR colours gets slightly redder (or cooler) with increasing $\mathrm{N_H}$ values.

We have also investigated the $L(\mathrm{IR})_{\mathrm{AGN}}$ dependence on the $\mathrm{N_H}$ value. As seen in the left panel of Fig. 10, while unobscured, and obscured AGN have a similar distribution CT-AGN have higher $L(\mathrm{IR})_{\mathrm{AGN}}$ values. The right panel of Fig. 10 shows that the infrared luminosity produced by the torus ,$L(\mathrm{IR})_{\mathrm{AGN(torus)}}$, is higher for CT-AGN.

5.4 Obscured/Compton-thick AGN selection by IR colours

We check many different colour-colour combinations including, optical, NIR, MIR and FIR, however we mostly find that CT AGNs distribute over a wide colour range similar to obscured and unobscured AGNs. In one particular colour-colour diagram with 9 μm - 22 μm versus 22 μm - 90 μm colours (Fig. 11) we find a distinct colour region which is mostly occupied by CT AGNs. This region is shown by the black dashed lines in Fig. 11. In this figure the unobscured, obscured and CT AGNs are shown as the grey triangles, black squares and red circles, respectively. The blue contours

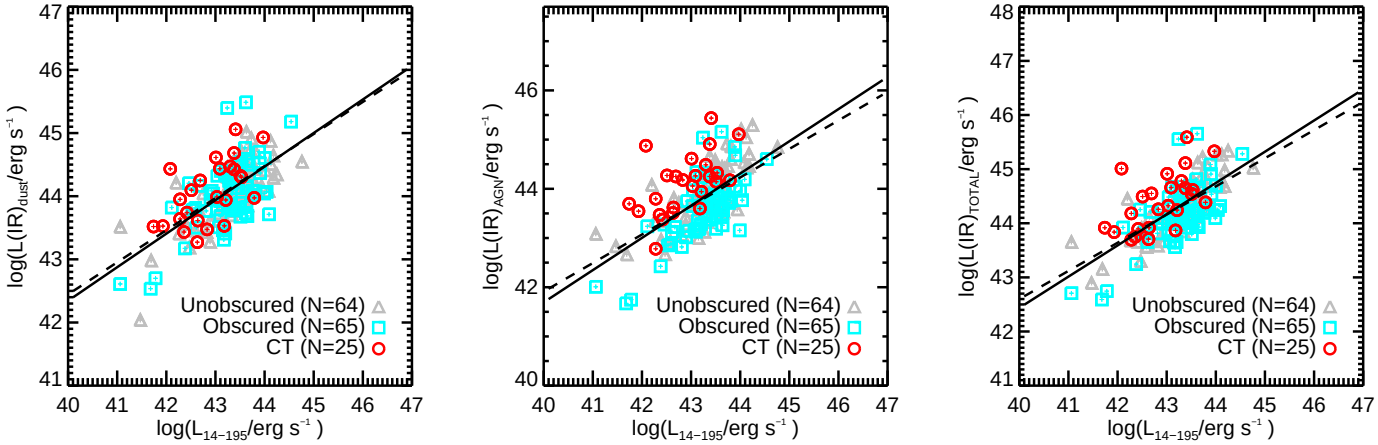

Figure 6. Relations between the 14-195 keV hard X-ray luminosity and $L_{\rm dust}$ (left panel), the pure AGN luminosity in the IR band, $L(\rm IR)_{\rm AGN}$ (middle panel) and the total IR luminosity (right panel) $L(\rm IR)_{\rm TOTAL}$. Triangles, squares and the circles represent the unobscured, obscured and CT AGN, respectively. The black solid lines show the best-fitting relationships for all sources. The dashed lines represent the best-fitting relationships for only obscured and CT AGN.

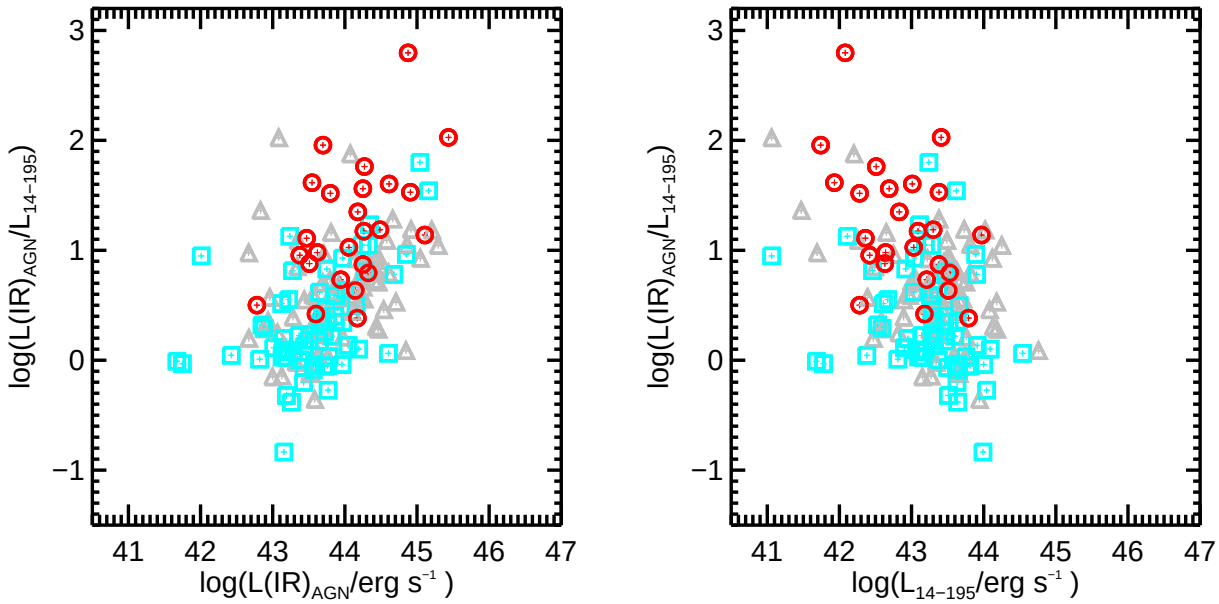

Figure 7. $L(\rm IR)_{\rm AGN}$ to L_{14-195} fraction as a function of $L(\rm IR)_{\rm AGN}$ (left panel) and L_{14-195} (right panel). See Fig. 6 for the symbol code.

are the 699 IR galaxies selected from the *AKARI* IR Galaxy catalogue of Kilerci Eser & Goto (2018) that have a similar redshift range of $z \leq 0.13$. We define the $[9\mu m - 22\mu m] > 2.0$ and $[22\mu m - 90\mu m] < 2.7$ as a new selection criteria for CT AGNs. The $[22\mu m - 90\mu m]$ colour separates AGN among IR galaxies, AGN have blue 22 μm - 90 μm colours. This is expected from the shallower slope of the $L_{\rm dust}$ and $L(\rm IR)_{\rm AGN}$ relationship (section 5.2.), considering the AGN IR emission traced by 22 μm and dust luminosity traced by 90 μm luminous AGN should give bluer $[22\mu m - 90\mu m]$ colours. *AKARI*/IRC S9W band cover silicate absorption feature at 9.7μm. As shown by Shi et al. (2006) the strength of 9.7μm absorption increases with higher $N_{\rm H}$. Therefore, the $[9\mu m - 22\mu m]$ colour is expected to be related to deep silicate absorption feature seen in heavily obscured AGN. $22\mu m$ is a measure of the MIR continuum. Once a source has a deep Silicate absorption, it will a have a fainter $9\mu m$ and a larger difference in the $[22\mu m - 90\mu m]$ colour. In Fig. 11 we have four CT AGN (NGC6240, NGC7479, NGC6552, NGC5643) that is used to define $[9\mu m - 22\mu m] > 2.0$ colour range. Stierwalt et al. (2013) represent *Spitzer* Infrared Spectrograph (IRS, Houck et al. 2004) spectra covering 5-38μm of NGC6240. According to their silicate depth and MIR slope measurements, NGC6240 shows a strong silicate absorption with a steep MIR slope. Stone et al. (2016) measure the strength of the $9.7\mu m$ silicate feature of NGC7479 from *Spitzer* MIR spectra. According to their measurements, NGC7479 has a strong silicate absorption feature. Shi et al. (2006) present *Spitzer* IRS spectrum of NGC5643, measure a deep silicate absorption feature. *Spitzer* low-resolution IRS-

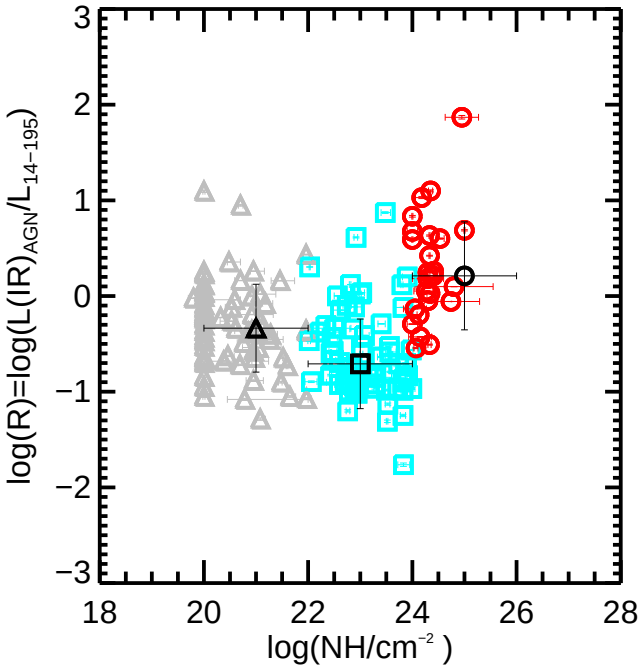

Figure 8. $R = L(\mathrm{IR})_{\mathrm{AGN}}/L(\mathrm{BOL})_{\mathrm{AGN}}$ versus N_H. See Fig. 6 for the symbol code. The black symbols represent the median R values in each N_H bin with the x-axis error bar showing the range of the N_H bin and the y-axis error bar showing the inter-percentage range with 68.2% of the unobscured, obscured and GT AGN samples.

LL spectrum of NGC6552 shows a rising MIR continuum between 15-35 μm (Jarrett et al. 2011). The *Spitzer* spectrum of NGC6552 do not cover $9\mu m$ range, therefore we do not have a measure for its silicate absorption strength. The MIR spectral measurements of NGC6240, NGC7479 and NGC5643 show evidence for relatively faint $9\mu m$ and relatively bright $22\mu m$ giving higher $[9\mu m - 22\mu m]$ colours.

We apply this criteria to the *AKARI* IR galaxy catalogue of Kilerci Eser & Goto (2018) and find 3 new CT AGNs candidates. These candidates are shown as cyan diamonds in Fig. 11. As a first step, we justify the nature of the CT AGN candidates based on the available public data sets and previous studies. The properties of the CT AGN candidates selected from the *AKARI* IR galaxy catalogue of Kilerci Eser & Goto (2018) is summarised in Table 4.

NGC 1614 is a well observed local LIRG. Its earlier X-ray observations with ASCA suggest the presence of an AGN based on the well fitted power-law in the 2-10 keV band (Risaliti et al. 2000). Although the weak hard X-ray emission indicates a Compton-thick AGN at the first place, the multi-wavelength observations in sub-millimetre (Xu et al. 2015), radio (Herrero-Illana et al. 2017) and X-rays (Pereira-Santaella et al. 2011; Herrero-Illana et al. 2014) do not support this. Xu et al. (2015) found that the amount of nuclear molecular gas and dust is much lower than that predicted for CT AGNs. According to Pereira-Santaella et al. (2011); Herrero-Illana et al. (2014) the hard and soft X-ray emission of this source can be explained by star-formation. As pointed out by (Pereira-Santaella et al. 2015), in case of a CT AGN the predicted 14-195 keV flux would be above the *Swift*/BAT survey sensitivity limit. Therefore, the non-detection of this source in the *Swift*/BAT survey (Oh et al. 2018) supports that it is not an CT AGN. Based on the current multi-wavelength available data we consider it as an unlikely/uncertain CT AGN candidate. But we caution that NGC1614 has not been observed with NuSTAR yet, and its high energy nature is still a subject for investigation.

NGC 4418 is a LIRG with a known dust embedded nuclear CT source. The nature of this source has been subject to many observations at different wavelengths and the presence of a CT AGN is highly favoured. Infrared observations (Roche et al. 1986; Spoon et al. 2001; Roche et al. 2015) of NGC 4418 show a deep silicate absorption at 10 μm and indicate a very heavily obscured, CT AGN. Submillimeter observations of NGC 4418 at high spatial resolution are also consistent with the presence of a CT AGN (Sakamoto et al. 2013). It's *Chandra*/Advanced CCD Imaging Spectrometer (ACIS) observations show a flat hard X-ray spectrum and imply the presence of a CT AGN, but due to the limited photon statistics this identification is considered as tentative (Maiolino et al. 2003). As pointed out by Roche et al. (2015), the non-detection of NGC 4418 by *Swift*/BAT survey (Baumgartner et al. 2013; Koss et al. 2013) is probably due to the extremely high levels of obscuration.

NGC 7714 is a well observed galaxy with a compact starburst nuclei (e.g., Gonzalez-Delgado et al. 1995; Smith et al. 2005). Smith et al. (2005) studied the X-ray emission from NGC 7714 with *Chandra*/ACIS. They report that the spectrum of the nuclear region can be fitted to a MEKAL function or an absorbed power-law function with a column density of $N_H = 2.2 \times 10^{21}$ cm^{-2}. Therefore, NGC 7714 possibly hosts an unobscured AGN.

This investigation shows us that our new colour selection criteria is successful to find at least one confirmed CT AGN. Since 9 μm - 22 μm colour of NGC 4418 is 3.32, we consider to take $[9\mu m - 22\mu m] > 3.0$ as a more reliable region that would avoid unobscured AGN selection. When we apply $[9\mu m - 22\mu m] > 3.0$ and $[22\mu m - 90\mu m] < 2.7$ as a criteria for a larger sample of combined *AKARI* and *WISE* sources without any selection criteria we find 341 candidates. These candidates are shown as the grey dots in Fig. 11. We investigate the nature of these 341 candidates in astronomical databases such as HEASARC[7], NASA/IPAC Extragalactic Database[8] (NED) and SIMBAD[9] (Wenger et al. 2000). We find that most of these sources are Galactic IR sources such as young stellar objects (YSOs), asymptotic giant branch (AGB) stars, Planetary Nebulae (PNe) and H II and star-forming regions. Among these 341 sources only 3 (IRAS06190+1040, IRAS21144+5430, Mrk34) are classified as a galaxy in the searched databases. Mrk34 is found to be a already known CT AGN in the literature (Gandhi et al. 2014). However, while IRAS06190+1040 is classified as a galaxy in NED it is classified as a Galactic star cluster by Froebrich (2017). IRAS21144+5430 is also classified as a galaxy in SDSS, but it is also classified as a H II region in SIMBAD. We also note that, IRAS06190+1040 and IRAS21144+5430 do not have archived X-ray observations for further investigation. We

[7] https://heasarc.gsfc.nasa.gov/cgi-bin/W3Browse/w3browse.pl
[8] http://nedwww.ipac.caltech.edu/.
[9] http://simbad.u-strasbg.fr/simbad/.

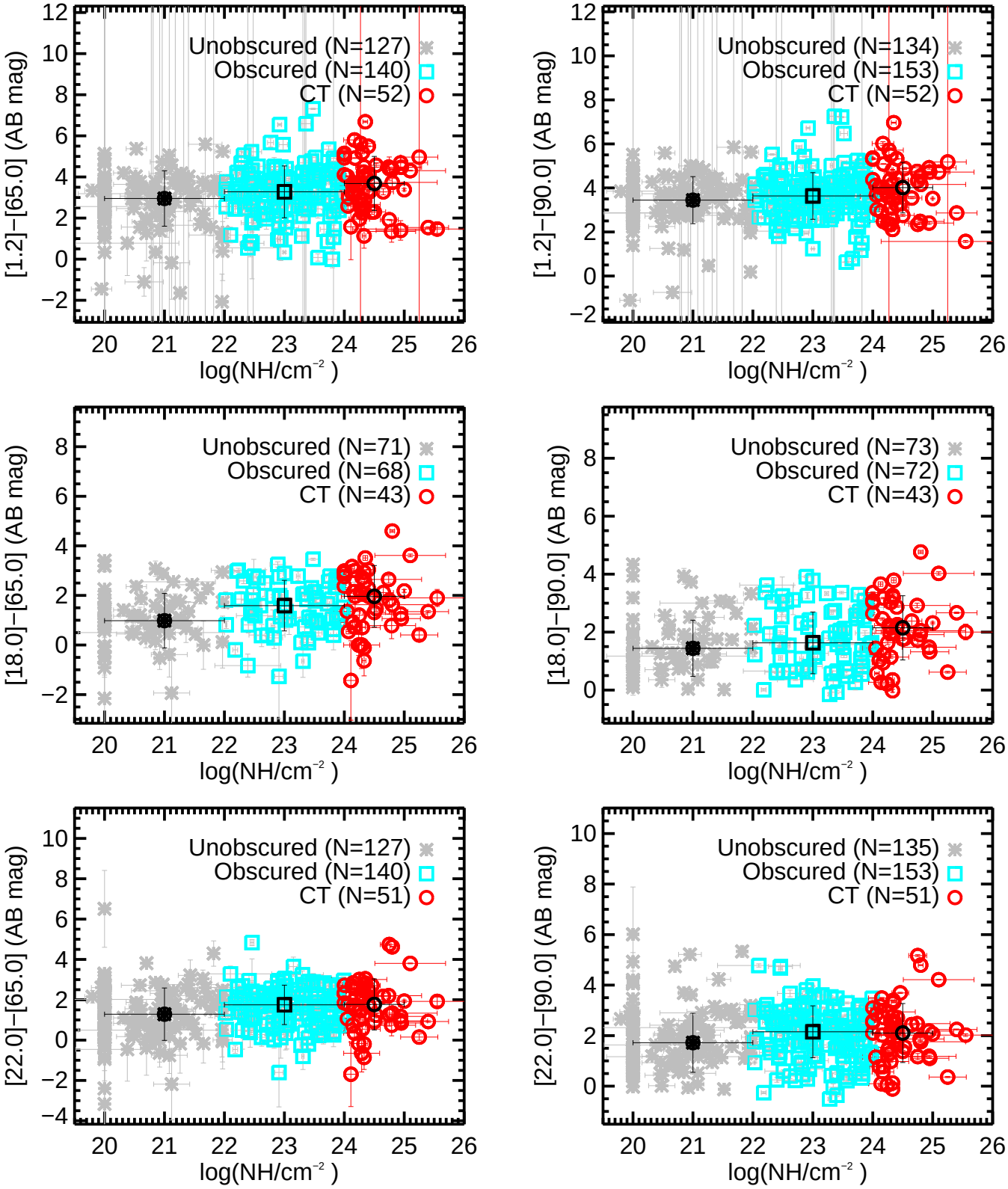

Figure 9. Infrared colour dependence on N_H. The black symbols represent the median colours in each N_H bin. Median 1.25μm - 65 μm, 1.25μm - 90 μm, 18 μm - 65 μm, 18 μm - 90 μm, 22 μm - 65 μm, 22 μm - 90 μm colours show an increasing trend with N_H.

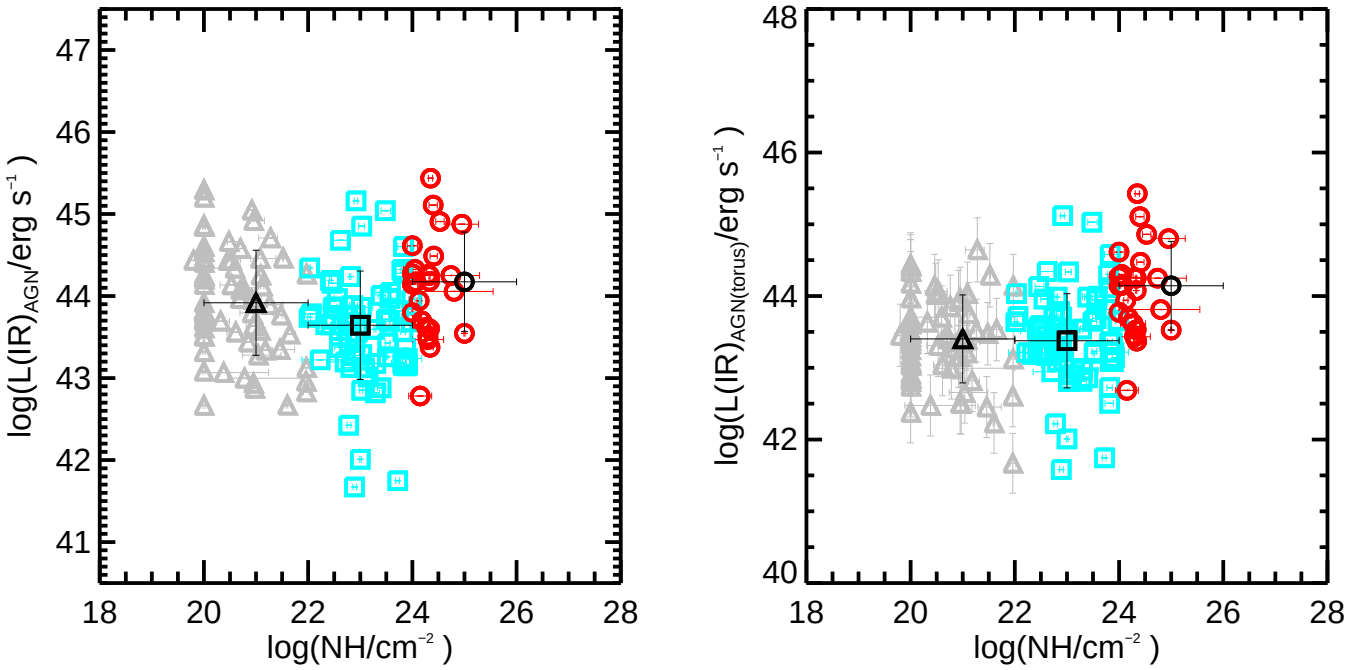

Figure 10. $L(\mathrm{IR})_{\mathrm{AGN}}$ (left) and $L(\mathrm{IR})_{\mathrm{AGN(torus)}}$ (right) versus $\mathrm{N_H}$. Compared to the unobscured and obscured AGN, median $L(\mathrm{IR})_{\mathrm{AGN}}$ and $L(\mathrm{IR})_{\mathrm{AGN(torus)}}$ luminosities are higher for CT-AGN (black circle).

Table 4. Properties of the CT AGN candidates. Columns: (1) Object name. (2) RA of the optical counterpart. (3) DEC of the optical counterpart. (4) Spectroscopic redshift of the optical counterpart. (5) [9μm - 22μm] colour. (6) [22μm - 90μm] colour. (7) Base 10 logarithm of the total infrared luminosity between 8 -1000μm. (8) Base 10 logarithm of the intrinsic Hydrogen column density in units of cm^{-2}. (9) X-ray reference for the adopted N_{H} value in column (8). (10) Our comment about the Compton-thick AGN candidate.

Name	RA (J2000.0) (deg)	Dec (J2000.0) (deg)	z	[9μm - 22μm] [AB] (mag)	[22μm - 90μm] [AB] (mag)	$\log(L_{IR}/L_{\odot})$	$\log(N_{\mathrm{H}})$	X-ray Ref.	Comment
(1)	(2)	(3)	(4)	(5)	(6)	(7)	(8)	(9)	(10)
NGC 1614	68.500	-8.579	0.016	2.04	2.03	11.60	21.58	Pereira-Santaella et al. (2011)	uncertain AGN
NGC 4418	186.727	-0.877	0.007	3.32	2.08	10.94	> 24	Maiolino et al. (2003)	CT AGN
NGC 7714	354.058	2.155	0.009	2.06	1.83	10.72	21.34	Smith et al. (2005)	unobscured AGN

find 3 sources that are classified as IR sources with X-ray observations, these are WISEA J162015.92-505621.8, 2MASS J16344841-4732432 and Allwise J181724.72-170628.1. X-ray observation of WISEA J162015.92-505621.8 show a weak X-ray source, but the quality of the available data does not allow for a reliable spectral analysis to measure $\mathrm{N_H}$. The available X-ray data of 2MASS J16344841-4732432 does not show a X-ray source. In the X-ray observation of Allwise J181724.72-170628.1 we identify a very weak X-ray source, the low S/N of the data does not allow to obtain a spectral fit. Based on the available X-ray data we can not confirm if these sources are CT AGN. However, all of these 3 sources are close to Galactic plane, and therefore they can also be Galactic IR sources.

6 CONCLUSIONS

We have analysed the broad-band SEDs of 68 unobscured, 65 obscured and 25 CT AGN from the UV to the far-IR by combining data from *GALEX*, SDSS, 2MASS, *WISE*, *AKARI* and *Herschel* surveys. We have constrained the parameters of the AGN component based on the AGN model Fritz et al. (2006). We have investigated a possible IR colour selection criteria for CT AGN based on *AKARI* and *WISE* photometric magnitudes and found a new promising colour selection criteria. The results of this work can be summarised as follows:

(i) The most important parameters to identify obscured/CT AGN from the SED analysis with CIGALE are the angle between equatorial axis and line of sight ψ, angular opening angle of the torus, θ. SED models with $\psi = 0.001°$ or $\psi = 10.0°$, and $\theta = 140$, are very likely to indicate an obscured or a CT AGN.

(ii) The comparison of average SEDs of the tree AGN populations show that the mid-IR SEDs are similar, the optical/UV region of the obscured/CT AGN is dominated by the host galaxy emission, and in the far-infrared region CT AGN show a stronger emission.

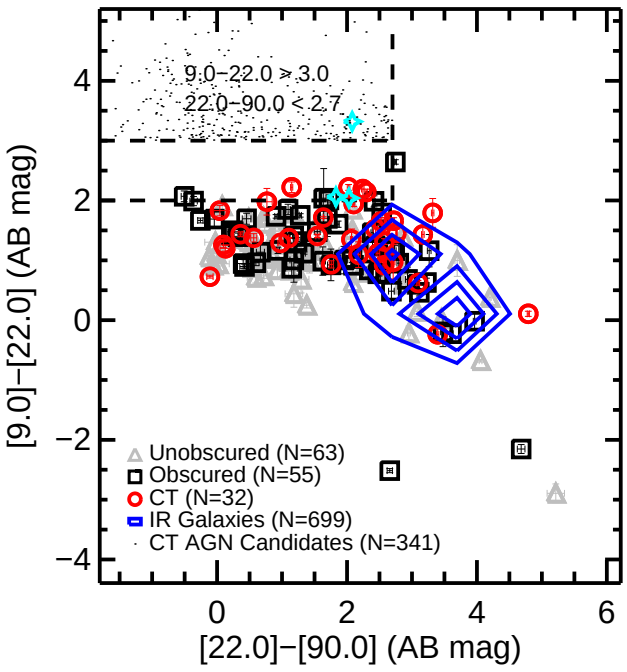

Figure 11. *AKARI*−*WISE* colours of X-ray selected AGNs with 9, 22, and 90 μm detections. The grey triangles are unobscured AGNs, the black squares are obscured AGNs and the red circles are Compton-thick AGNs. The blue contours represent 699 IR galaxies from *AKARI* IR Galaxy catalogue of Kilerci Eser & Goto (2018) within the $z \leq 0.13$ limit that have detections at 9, 22, and 90 μm bands. Cyan diamonds represent the three CT AGN candidates selected from *AKARI* IR galaxy catalogue of Kilerci Eser & Goto (2018) based on the $[9\mu m - 22\mu m] > 2.0$ and $[22\mu m - 90\mu m] < 2.7$ selection criteria.

(iii) We identify 27 strong AGN luminosity dominated sources among the unobscured, obscured and CT AGN based on the $frac_{\rm AGN}$ obtained by the SED fitting. These represent AGN luminosity dominated UV to FIR SEDs. We find that while unobscured and obscured AGN have a similar $frac_{\rm AGN}$ distribution, CT AGN have higher $frac_{\rm AGN}$ values.

(iv) We find a moderately strong correlation luminosity correlations between $L_{\rm dust}$-L_{14-195}, $L({\rm IR})_{\rm AGN}$-L_{14-195} and $L({\rm IR})_{\rm AGN}$-L_{14-195}. We quantify the relationships between these separated IR luminosities and the ultra hard X-ray luminosity for the hard X-ray selected AGN from *Swift*-BAT 105-month survey catalogue.

(v) We compare average covering factor ($R = L({\rm IR})_{\rm AGN}/L({\rm BOL})_{\rm AGN}$) for unobscured, obscured and CT. We show that CT AGN have larger covering factors compared to the obscured and unobscured AGN.

(vi) We show that the median 1.25μm - 65 μm, 1.25μm - 90 μm, 18 μm - 65 μm, 18 μm - 90 μm, 22 μm - 65 μm, 22 μm - 90 μm colours of the unobscured, obscured and CT AGN have an increasing trend with $N_{\rm H}$. We show that MIR-FIR colours have a tendency to become redder (or cooler) with increasing $N_{\rm H}$.

(vii) We find that CT AGN have higher $L({\rm IR})_{\rm AGN}$ and $L({\rm IR})_{\rm AGN(torus)}$ compared to obscured and unobscured AGN.

(viii) We present a new CT AGN selection criteria as $9-22 > 3.0$ and $22-90 < 2.7$. As a result of this criteria we find two known CT AGN (NGC4418 and Mrk34) that are not included in *Swift*-BAT sample. Due to the limited number of sources detected in 9μm we could not find any new CT AGN. We conclude that MIR photometric bands covering 9.7μm silicate absorption and MIR continuum can be used as a new tool to select the most heavily obscured CT AGN.

Acknowledgements

We thank the referee for many insightful comments. EKE acknowledges a post-doctoral fellowship support from TUBİTAK-BİDEB through 2218 program. We thank Denis Burgarella for useful discussion about CIGALE. TG acknowledges the support by the Ministry of Science and Technology of Taiwan through grant NSC 108-2628-M-007-004-MY3. This research is based on observations with AKARI, a JAXA project with the participation of ESA. This publication makes use of data products from the Wide-field Infrared Survey Explorer, which is a joint project of the University of California, Los Angeles, and the Jet Propulsion Laboratory/California Institute of Technology, funded by the National Aeronautics and Space Administration. *Herschel* is an ESA space observatory with science instruments provided by European-led Principal Investigator consortia and with important participation from NASA. This publication makes use of data products from the Two Micron All Sky Survey, which is a joint project of the University of Massachusetts and the Infrared Processing and Analysis Center/California Institute of Technology, funded by the National Aeronautics and Space Administration and the National Science Foundation.

REFERENCES

Abolfathi B., et al., 2018, ApJS, 235, 42
Alonso-Herrero A., et al., 2006, ApJ, 640, 167
Antonucci R., 1993, ARA&A, 31, 473
Arnaud K. A., 1996, in Jacoby G. H., Barnes J., eds, Astronomical Society of the Pacific Conference Series Vol. 101, Astronomical Data Analysis Software and Systems V. p. 17
Asmus D., Gandhi P., Smette A., Hönig S. F., Duschl W. J., 2011, A&A, 536, A36
Asmus D., Gandhi P., Hönig S. F., Smette A., Duschl W. J., 2015, MNRAS, 454, 766
Assef R. J., et al., 2013, ApJ, 772, 26
Assef R. J., et al., 2015, ApJ, 804, 27
Baloković M., et al., 2014, ApJ, 794, 111
Barthelmy S. D., et al., 2005, Space Sci. Rev., 120, 143
Baumgartner W. H., et al., 2013, ApJS, 207, 19
Bianchi L., Shiao B., Thilker D., 2017, ApJS, 230, 24
Boquien M., et al., 2019, A&A, 622, A103
Brandt W. N., Alexander D. M., 2015, A&ARv, 23, 1
Cardelli J. A., Clayton G. C., Mathis J. S., 1989, ApJ, 345, 245
Charlot S., Fall S. M., 2000, ApJ, 539, 718
Chen C.-T. J., Hickox R. C., Alberts S., Harrison C. M., et al., 2015, ApJ, 802, 50
Chen C.-T. J., et al., 2017, ApJ, 837, 145
Clements et al., 2019, PASJ, 71, 7
Cutri R. M., et al., 2003, VizieR Online Data Catalog, 2246
Cutri R. M., et al., 2013, VizieR Online Data Catalog, 2328
Czerny B., Elvis M., 1987, ApJ, 321, 305
Doi Y., et al., 2015, PASJ, 67, 50

Done C., Davis S. W., Jin C., Blaes O., Ward M., 2012, MNRAS, 420, 1848
Donley J. L., Rieke G. H., Pérez-González P. G., Rigby J. R., Alonso-Herrero A., 2007, ApJ, 660, 167
Donley J. L., Rieke G. H., Pérez-González P. G., Barro G., 2008, ApJ, 687, 111
Donley J. L., et al., 2012, ApJ, 748, 142
Draine B. T., et al., 2014, ApJ, 780, 172
Elitzur M., 2012, ApJ, 747, L33
Fiore F., et al., 2009, ApJ, 693, 447
Fritz J., Franceschini A., Hatziminaoglou E., 2006, MNRAS, 366, 767
Froebrich D., 2017, MNRAS, 469, 1545
Fruscione A., et al., 2006, in Society of Photo-Optical Instrumentation Engineers (SPIE) Conference Series. p. 62701V, doi:10.1117/12.671760
Fukazawa Y., Iyomoto N., Kubota A., Matsumoto Y., Makishima K., 2001, A&A, 374, 73
Gabriel C., et al., 2004, in Ochsenbein F., Allen M. G., Egret D., eds, Astronomical Society of the Pacific Conference Series Vol. 314, Astronomical Data Analysis Software and Systems (ADASS) XIII. p. 759
Gandhi P., et al., 2009, A&A, 502, 457
Gandhi P., et al., 2014, ApJ, 792, 117
Gandhi P., et al., 2015, MNRAS, 449, 1845
Gandhi P., et al., 2017, MNRAS, 467, 4606
García-Bernete I., et al., 2016, MNRAS, 463, 3531
García-Burillo S., et al., 2016, ApJ, 823, L12
Garmire G. P., Bautz M. W., Ford P. G., Nousek J. A., Ricker George R. J., 2003, in Truemper J. E., Tananbaum H. D., eds, Society of Photo-Optical Instrumentation Engineers (SPIE) Conference Series Vol. 4851, X-Ray and Gamma-Ray Telescopes and Instruments for Astronomy.. pp 28–44, doi:10.1117/12.461599
Gehrels N., et al., 2004, ApJ, 611, 1005
Giustini M., et al., 2017, A&A, 597, A66
Gonzalez-Delgado R. M., Perez E., Diaz A. I., Garcia-Vargas M. L., Terlevich E., Vilchez J. M., 1995, ApJ, 439, 604
Griffin M. J., et al., 2010, A&A, 518, L3
Herrero-Illana R., et al., 2014, ApJ, 786, 156
Herrero-Illana R., Alberdi A., Pérez-Torres M. Á., Alonso-Herrero A., González-Millán D., Pereira-Santaella M., 2017, MNRAS, 470, L112
Hickox R. C., Alexander D. M., 2018, ARA&A, 56, 625
Hickox R. C., et al., 2007, ApJ, 671, 1365
Hickox R. C., Myers A. D., Greene J. E., Hainline K. N., Zakamska N. L., DiPompeo M. A., 2017, ApJ, 849, 53
Hiner K. D., et al., 2009, ApJ, 706, 508
Hönig S. F., Beckert T., 2007, MNRAS, 380, 1172
Hopkins P. F., Hernquist L., Cox T. J., Kereš D., 2008, ApJS, 175, 356
Horst H., Gandhi P., Smette A., Duschl W. J., 2008, A&A, 479, 389
Houck J. R., et al., 2004, ApJS, 154, 18
Huang T.-C., Goto T., Hashimoto T., Oi N., Matsuhara H., 2017, MNRAS, 471, 4239
Ichikawa K., et al., 2012, ApJ, 754, 45
Ichikawa K., et al., 2017, ApJ, 835, 74
Ichikawa K., et al., 2019, ApJ, 870, 31
Ishihara D., et al., 2010, A&A, 514, A1
Iwasawa K., U V., Mazzarella J. M., Medling A. M., Sanders D. B., Evans A. S., 2018, A&A, 611, A71
Jansen F., et al., 2001, Astronomy and Astrophysics, 365, L1
Jarrett T. H., Chester T., Cutri R., Schneider S., Skrutskie M., Huchra J. P., 2000, AJ, 119, 2498
Jarrett T. H., et al., 2011, ApJ, 735, 112
Jarrett T. H., et al., 2013, AJ, 145, 6
Jin C., Ward M., Done C., Gelbord J., 2012, MNRAS, 420, 1825
Kelly B. C., 2007, ApJ, 665, 1489
Kilerci Eser E., Goto T., 2018, MNRAS, 474, 5363
Koss M., et al., 2013, ApJ, 765, L26
Koss M. J., et al., 2016, ApJ, 824, L4
Koss M., et al., 2017, ApJ, 850, 74
Krabbe A., Böker T., Maiolino R., 2001, ApJ, 557, 626
Lacy M., et al., 2004, ApJS, 154, 166
Lansbury G. B., et al., 2014, ApJ, 785, 17
Lansbury G. B., et al., 2017, ApJ, 846, 20
Lawrence A., 1991, MNRAS, 252, 586
Levenson N. A., Radomski J. T., Packham C., Mason R. E., Schaefer J. J., Telesco C. M., 2009, ApJ, 703, 390
Lutz D., Maiolino R., Spoon H. W. W., Moorwood A. F. M., 2004, A&A, 418, 465
Maiolino R., et al., 1998, A&A, 338, 781
Maiolino R., et al., 2003, MNRAS, 344, L59
Malizia A., et al., 2007, ApJ, 668, 81
Malizia A., et al., 2008, MNRAS, 389, 1360
Malizia A., et al., 2011, in Extreme and Variable High Energy Sky (Extremesky 2011). p. 48
Malizia A., et al., 2012, MNRAS, 426, 1750
Maraston C., 2005, MNRAS, 362, 799
Marchesi S., Ajello M., Marcotulli L., Comastri A., Lanzuisi G., Vignali C., 2018, ApJ, 854, 49
Marchesi S., Ajello M., Zhao X., Comastri A., La Parola V., Segreto A., 2019, arXiv e-prints, p. arXiv:1907.09193
Marconi A., Risaliti G., Gilli R., Hunt L. K., Maiolino R., Salvati M., 2004, MNRAS, 351, 169
Martin D. C., et al., 2005, ApJ, 619, L1
Mason R. E., et al., 2012, AJ, 144, 11
Mateos S., et al., 2012, MNRAS, 426, 3271
Mateos S., et al., 2013, MNRAS, 434, 941
Mateos S., et al., 2015, MNRAS, 449, 1422
Mateos S., et al., 2017, ApJ, 841, L18
Matsuoka K., Woo J.-H., 2015, ApJ, 807, 28
Matsuta K., et al., 2012, ApJ, 753, 104
Matt G., Bianchi S., Guainazzi M., Barcons X., Panessa F., 2012, A&A, 540, A111
Mehdipour M., et al., 2011, A&A, 534, A39
Mehdipour M., et al., 2015, A&A, 575, A22
Meléndez M., Mushotzky R. F., Shimizu T. T., Barger A. J., Cowie L. L., 2014, ApJ, 794, 152
Mewe R., Gronenschild E. H. B. M., van den Oord G. H. J., 1985, A&AS, 62, 197
Mullaney J. R., Alexander D. M., Goulding A. D., Hickox R. C., 2011, MNRAS, 414, 1082
Mushotzky R. F., Shimizu T. T., Meléndez M., Koss M., 2014, ApJ, 781, L34
Netzer H., 2009, MNRAS, 399, 1907
Noll S., Burgarella D., Giovannoli E., Buat V., Marcillac D., Muñoz-Mateos J. C., 2009, A&A, 507, 1793
Oh K., et al., 2018, ApJS, 235, 4
Pappa A., Georgantopoulos I., Ward M., Zezas A. L., 2002, MNRAS, 336, 714
Pearson K., 1896, Philosophical Transactions of the Royal Society of London S 187, 253
Pereira-Santaella M., et al., 2011, A&A, 535, A93
Pereira-Santaella M., et al., 2015, MNRAS, 454, 3679
Pian E., Romano P., Maoz D., Cucchiara A., Pagani C., La Parola V., 2010, MNRAS, 401, 677
Pilbratt G. L., et al., 2010, A&A, 518, L1
Poglitsch A., et al., 2010, A&A, 518, L2
Ramos Almeida C., Pérez García A. M., Acosta-Pulido J. A., Rodríguez Espinosa J. M., 2007, AJ, 134, 2006
Ricci C., et al., 2017a, ApJS, 233, 17
Ricci C., et al., 2017b, Nature, 549, 488
Risaliti G., Gilli R., Maiolino R., Salvati M., 2000, A&A, 357, 13

Roche P. F., Aitken D. K., Smith C. H., James S. D., 1986, MNRAS, 218, 19P
Roche P. F., Alonso-Herrero A., Gonzalez-Martin O., 2015, MNRAS, 449, 2598
Rovilos E., et al., 2014, MNRAS, 438, 494
Sakamoto K., et al., 2013, ApJ, 764, 42
Salpeter E. E., 1955, ApJ, 121, 161
Sanders D. B., Phinney E. S., Neugebauer G., Soifer B. T., Matthews K., 1989, ApJ, 347, 29
Sazonov S., et al., 2012, ApJ, 757, 181
Schlegel D. J., Finkbeiner D. P., Davis M., 1998, ApJ, 500, 525
Serra P., et al., 2011, ApJ, 740, 22
Shakura N. I., Sunyaev R. A., 1973, A&A, 24, 337
She R., Ho L. C., Feng H., 2017, ApJ, 835, 223
Shi Y., et al., 2006, ApJ, 653, 127
Shimizu T. T., et al., 2016, MNRAS, 456, 3335
Shu X. W., Wang J. X., Jiang P., Fan L. L., Wang T. G., 2007, ApJ, 657, 167
Simpson C., 2005, MNRAS, 360, 565
Skrutskie M. F., et al., 2006, AJ, 131, 1163
Smith B. J., Struck C., Nowak M. A., 2005, AJ, 129, 1350
Spoon H. W. W., Keane J. V., Tielens A. G. G. M., Lutz D., Moorwood A. F. M., 2001, A&A, 365, L353
Stern D., et al., 2005, ApJ, 631, 163
Stern D., et al., 2012, ApJ, 753, 30
Stierwalt S., et al., 2013, ApJS, 206, 1
Stone M., Veilleux S., Meléndez M., Sturm E., Graciá-Carpio J., González-Alfonso E., 2016, ApJ, 826, 111
Strauss M. A., et al., 2002, AJ, 124, 1810
Suganuma M., et al., 2006, ApJ, 639, 46
Telfer R. C., Zheng W., Kriss G. A., Davidsen A. F., 2002, ApJ, 565, 773
Treister E., et al., 2010, ApJ, 722, L238
Tueller J., et al., 2008, ApJ, 681, 113
Ueda Y., Akiyama M., Hasinger G., Miyaji T., Watson M. G., 2014, ApJ, 786, 104
Verner D. A., Ferland G. J., Korista K. T., Yakovlev D. G., 1996, ApJ, 465, 487
Weisskopf M. C., Tananbaum H. D., Van Speybroeck L. P., O'Dell S. L., 2000, in Truemper J. E., Aschenbach B., eds, Society of Photo-Optical Instrumentation Engineers (SPIE) Conference Series Vol. 4012, X-Ray Optics, Instruments, and Missions III. pp 2–16 (arXiv:astro-ph/0004127), doi:10.1117/12.391545
Wenger M., et al., 2000, A&AS, 143, 9
Wilms J., Allen A., McCray R., 2000, ApJ, 542, 914
Wright E. L., et al., 2010, AJ, 140, 1868
Xu C. K., et al., 2015, ApJ, 799, 11
Yamamura I., Makiuchi S., Koga T., AKARI Team 2018, in Ootsubo T., Yamamura I., Murata K., Onaka T., eds, The Cosmic Wheel and the Legacy of the AKARI Archive: From Galaxies and Stars to Planets and Life. pp 227–230
York D. G., et al., 2000, AJ, 120, 1579
Zhang J. S., et al., 2006, A&A, 450, 933
Zheng W., Kriss G. A., Telfer R. C., Grimes J. P., Davidsen A. F., 1997, ApJ, 475, 469
de Rosa A., et al., 2012, MNRAS, 420, 2087

APPENDIX A: X-RAY SPECTRAL ANALYSIS

For *XMM-Newton* (Jansen et al. 2001) we mostly used EPIC-pn camera data. Only for ESO450-16 we used both EPIC-pn and EPIC-MOS data. We calibrated the data using SAS v15.0.0 (Gabriel et al. 2004) and the calibration files as of 01/01/2019 using *epproc* package. We extracted source spectra using a circular region with a radius of about 32 arcsec. We extracted the background spectra from a nearby (located on the same CCD) uncontaminated larger circular region. Response and ancillary response files are generated using the *rmfgen* and *arfgen* tools.

For one source we used *Chandra*/ACIS (Weisskopf et al. 2000; Garmire et al. 2003) data. *Chandra* data were reduced using CIAO v.4.9 (Fruscione et al. 2006) following standard procedures. We used *chandra_repro* task to reprocess the data. The spectra were extracted using *specextract* tool from a circular aperture of 10 arcsec radius. Background spectra were extracted using a larger source free nearby circular region.

We performed X-ray spectral fitting using the XSPEC V. 12.10.1 software (Arnaud 1996). We adopted Verner cross-section (Verner et al. 1996) and Wilm abundance (Wilms et al. 2000) in TBABS model to account for the Galactic absorption. Intrinsic absorption also modelled with TBABS. We grouped all spectra to have at least 50 counts per channel (only for 2MASX J08384815+0407340 we used 40 counts) and used χ^2 statistics. We fit the X-ray spectra in the 0.4 - 9.0 keV energy range, only in a few cases we had to narrow the used energy range due to the source brightness as shown in Fig. A1. In order to measure the intrinsic N_H value the spectra are fitted using a single power-law modified by Galactic absorption plus an intrinsic absorption at the redshift of each source. During the spectral fitting process the power-law normalisation and the intrinsic column density were always left as free parameters. For 2MASXJ16510578-0129258, CGCG081-001 and MCG+00-58-028 the slope of the power-law was left as a free parameter. As shown by Marchesi et al. (2018) fixing the photon index to the typical AGN value of $\Gamma \sim 1.7$ in low-quality 2 keV-10 keV spectra gives better intrinsic N_H measurements. Therefore, for 2MASXJ08384815+0407340, IC-588, ESO439-G009, and NGC5940 we fixed photon index to $\Gamma = 1.7$ or $\Gamma = 1.8$. For ESO450-16 we limited the slope of the power-law between 1.0 and 2.0, for this source fixing Γ to be 1.7 does not give a statistically acceptable fit. For these sources when necessary, we also added a Gaussian line to the power-law model in order to obtain a better fit result. For IC-588, ESO439-G009 and NGC5940 we used the additional MEKAL model (Mewe et al. 1985) to model the soft X-rays below 1 keV. The obtained spectral parameters from the spectral fitting are listed in Table A1. We show the best-fitting *Chandra* and *XMM-Newton* X-ray spectra in Figure A1. As a result of our analysis we classify 2MASXJ08384815+0407340, IC-588, 2MASXJ16510578-0129258, MCG+00-58-028 as obscured AGN and ESO439-G009, NGC5940, ESO450-16, CGCG081-001 as unobscured AGN.

This paper has been typeset from a TEX/LATEX file prepared by the author.

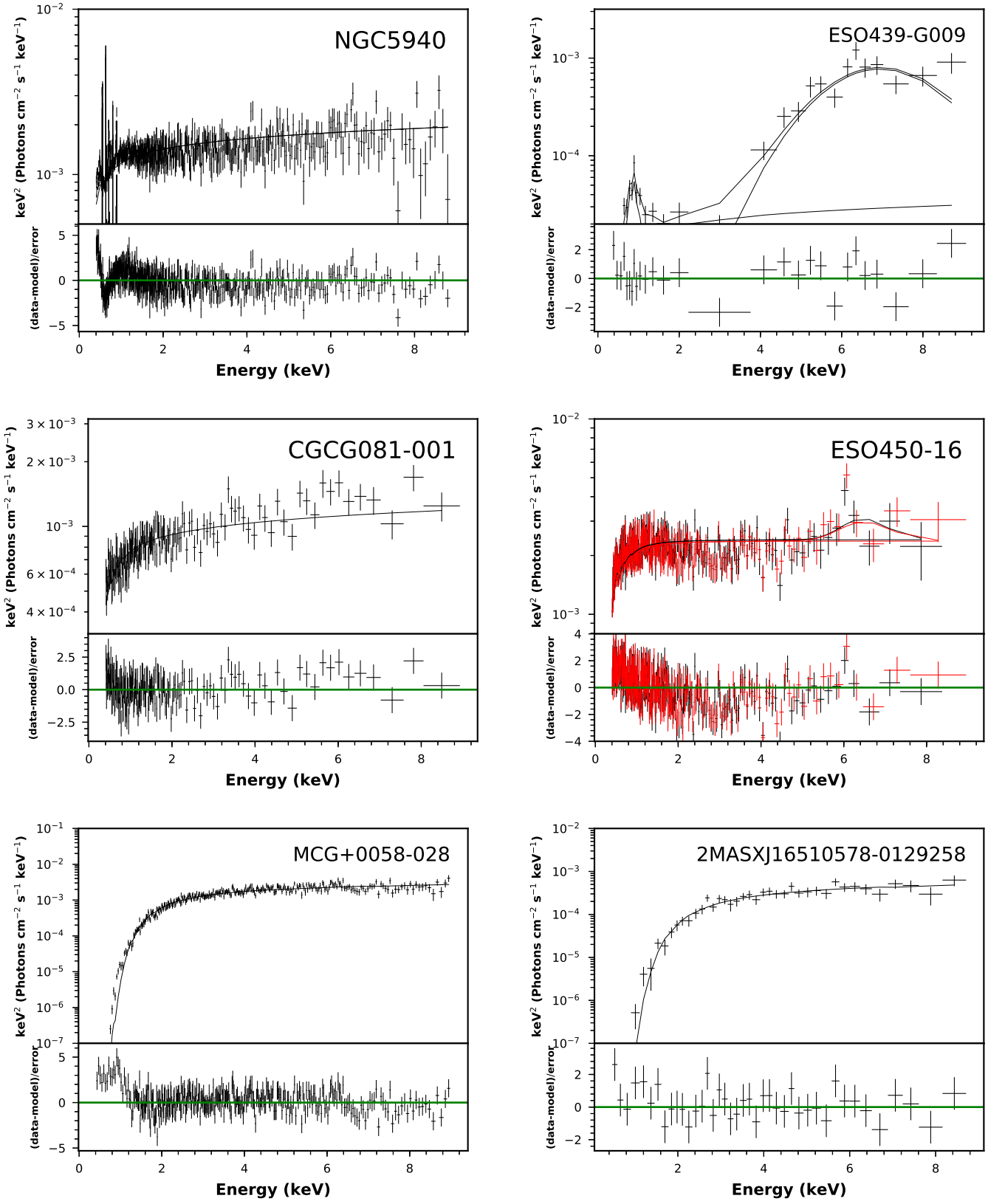

Figure A1. The best-fitting spectra of AGN observed with *XMM-Newton* and *Chandra*. For seven sources we use *XMM-Newton* EPIC-pn data and only for ESO450-16 we used both EPIC-pn and EPIC-MOS (shown in red) data.

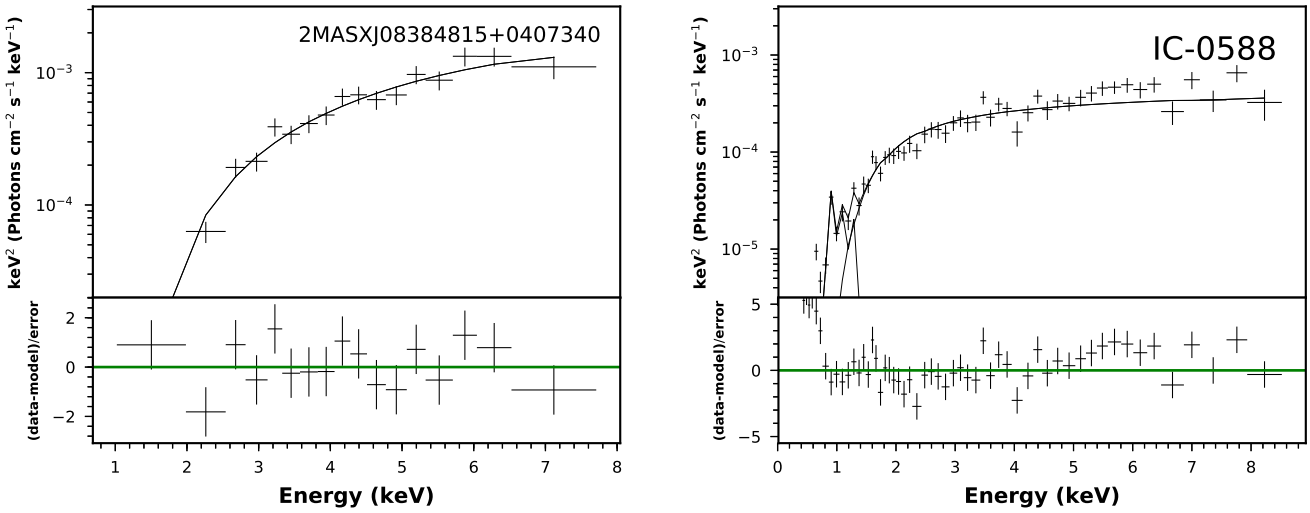

Figure A1 – *continued*

Table A1. X-ray spectral analysis results. Columns: (1) Object name. (2) X-ray facility. (3) Galactic N_H. (4) Measured intrinsic N_H. (5) Temperature kT in keV of the MEKAL component. (6) Line energy of the simple gaussian profile in keV. (7) Power-law photon index. (8) Reduced chi-squared (degrees of freedom).

Source name	Facility	N_{H_Gal} (10^{20} cm^{-2})	N_{H_int} (10^{22} cm^{-2})	kT (keV)	Line energy (keV)	Γ	χ^2 (d.o.f)
(1)	(2)	(3)	(4)	(5)	(6)	(7)	(8)
2MASXJ08384815+0407340	*Chandra*	2.68	$5.09^{2.61}_{0.90}$		$0.20^{0.90}_{2.45}$	1.7	1.20 (12)
IC-588	*XMM-Newton*	1.71	$2.88^{0.5}_{1.90}$	$0.08^{0.01}_{0.08}$		1.7	4.34 (51)
ES0439-G009	*XMM-Newton*	5.44	≤ 0.01	$0.68^{0.07}_{0.05}$	$6.40^{0.17}_{0.15}$	1.7	1.88 (21)
NGC5940	*XMM-Newton*	3.95	≤ 0.01	$0.23^{0.01}_{0.01}$		1.8	1.70 (555)
ESO450-16	*XMM-Newton*	7.46	≤ 0.01		$6.40^{0.15}_{0.21}$	$2.0^{0.2}_{0.2}$	1.65 (558)
CGCG081-001	*XMM-Newton*	4.43	≤ 0.01			$1.83^{0.16}_{0.15}$	1.14 (171)
2MASXJ16510578-0129258	*XMM-Newton*	7.80	$5.39^{1.01}_{0.96}$			$1.50^{0.23}_{0.22}$	0.93 (38)
MCG+00-58-028	*XMM-Newton*	3.92	$3.29^{0.12}_{0.12}$			$1.59^{0.04}_{0.04}$	1.63 (327)